Dissolution susceptibility of glass-like carbon versus crystalline graphite in high-pressure aqueous fluids and implications for the behavior of organic matter in subduction zones

Simone Tumiati [a,*], Carla Tiraboschi [a,b], Francesca Miozzi [a,c]
Alberto Vitale-Brovarone [c,d], Craig E. Manning [e], Dimitri A. Sverjensky [f],
Sula Milani [a], Stefano Poli [a]

[a] *Dipartimento di Scienze della Terra, Università degli Studi di Milano, via Mangiagalli 34, 20133 Milano, Italy*
[b] *Institut für Mineralogie, Universität Münster, Corrensstrasse 24, 48149 Münster, Germany*
[c] *Sorbonne Université, Muséum National d'Histoire Naturelle, UMR CNRS 7590, IRD, Institut de Minéralogie, de Physique des Matériaux et de Cosmochimie, IMPMC, 75005 Paris, France*
[d] *Dipartimento di Scienze della Terra, Università degli Studi di Torino, via Valperga Caluso 35, 10125 Torino, Italy*
[e] *Department of Earth, Planetary and Space Sciences, University of California, Los Angeles, CA 90095-1567, USA*
[f] *Department of Earth & Planetary Sciences, Johns Hopkins University, Baltimore, MD 21218, USA*

Abstract

Organic matter, showing variable degrees of crystallinity and thus of graphitization, is an important source of carbon in subducted sediments, as demonstrated by the isotopic signatures of deep and ultra-deep diamonds and volcanic emissions in arc settings. In this experimental study, we investigated the dissolution of sp^2 hybridized carbon in aqueous fluids at 1 and 3 GPa, and 800 °C, taking as end-members (i) crystalline synthetic graphite and (ii) X-ray amorphous glass-like carbon. We chose glass-like carbon as an analogue of natural "disordered" graphitic carbon derived from organic matter, because unlike other forms of poorly ordered carbon, it does not undergo any structural modification at the investigated experimental conditions, allowing approach to thermodynamic equilibrium. Textural observations, Raman spectroscopy, synchrotron X-ray diffraction and dissolution susceptibility of char produced by thermal decomposition of glucose (representative of non-transformed organic matter) at the same experimental conditions support this assumption. The redox state of the experiments was buffered at ΔFMQ $\approx$ –0.5 using double capsules and either fayalite-magnetite-quartz (FMQ) or nickel-nickel oxide (NNO) buffers. At the investigated P–T–fO$_2$ conditions, the dominant aqueous dissolution product is carbon dioxide, formed by oxidation of solid carbon. At 1 GPa and 800 °C, oxidative dissolution of glass-like carbon produces 16–19 mol% more carbon dioxide than crystalline graphite. In contrast, fluids interacting with glass-like carbon at the higher pressure of 3 GPa show only a limited increase in CO$_2$ (fH$_2^{NNO}$) or even a lower CO$_2$ content (fH$_2^{FMQ}$) with respect to fluids interacting with crystalline graphite. The measured fluid compositions allowed retrieval of the difference in Gibbs free energy (ΔG) between glass-like carbon and graphite, which is +1.7(1) kJ/mol at 1 GPa–800 °C and +0.51(1) kJ/mol (fH$_2^{NNO}$) at 3 GPa–800 °C. Thermodynamic modeling suggests that the decline in dissolution susceptibility at high pressure is related to the higher compressibility of glass-like carbon with respect to crystalline graphite, resulting in G–P curves crossing at about 3.4 GPa at 800 °C, close to the graphite–diamond transition. The new experimental data suggest that, in the presence of aqueous fluids that flush

---

* Corresponding author.
  E-mail address: simone.tumiati@unimi.it (S. Tumiati).

subducted sediments, the removal of poorly crystalline "disordered" graphitic carbon is more efficient than that of crystalline graphite. This occurs especially at shallow levels of subduction zones, where the difference in free energy is higher and the availability of poorly organized metastable carbonaceous matter and of aqueous fluids produced by devolatilization of the downgoing slab is maximized. At depths greater than 110 km, the small differences in ΔG imply that there is minimal energetic drive for transforming "disordered" graphitic carbon to ordered graphite; "disordered" graphitic carbon could even be energetically slightly favored in a narrow P interval.

1. INTRODUCTION

The carbon isotopic signature of the upper mantle, transition zone and lower mantle (Stachel et al., 2002; Cartigny et al., 2004; Palot et al., 2014), and of gaseous CO_2 emitted from arc volcanoes (Mason et al., 2017) suggests that organic matter subducted within sediments displays a major role in the deep carbon cycle (Hayes and Waldbauer, 2006). The dissolution of graphitic carbon in aqueous fluids due to oxidation or reduction processes (Connolly and Cesare, 1993; Connolly, 1995; Zhang et al., 2018; Tumiati and Malaspina, 2019) is of primary importance as it governs the removal of organic matter from the sediments flushed by fluids released from the dehydrating subducted plate (Schmidt and Poli, 2013). In contrast to carbonates (e.g., Kelemen and Manning, 2015), graphite has long been considered to represent a refractory sink of carbon in the subducting slab (Plank and Manning, 2019), showing low solubility in metamorphic fluids (Connolly and Cesare, 1993) and silicate melts (Duncan and Dasgupta, 2017). However, recent thermodynamic models and experiments suggest that graphite can be readily dissolved in subduction fluids (Manning et al., 2013), stressing for instance the importance of pH (Sverjensky et al., 2014a,b) and of dissolved silica (Tumiati et al., 2017). However, it is still not known how graphite crystallinity might affect the compositions of COH fluids in subduction zones.

Carbonaceous material in sedimentary rocks metamorphosed under temperature and pressure conditions characteristic of subduction zones exhibit a progressive increase in crystallinity (e.g., Beyssac et al., 2002). Besides exceptional preservations of amorphous-like carbon in some metamorphic rocks (Bernard et al., 2007), carbonaceous material metamorphosed under prograde temperature increase to about 550 °C is characterized by a variety of turbostratic structures, from poorly crystallized to almost crystalline, that are commonly referred to as disordered graphitic carbon (Beyssac and Rumble, 2014; Aoya et al., 2010). Carbonaceous material in high-temperature and ultra-high-pressure terranes is instead characterized by rather crystalline graphite (Beyssac et al., 2002). Thus, disordered graphitic carbon should represent the most common form of carbonaceous material under forearc to sub-arc metamorphic conditions where large amounts of aqueous fluids are released from the slab.

Crystalline (ordered) graphite is crystallographically defined by an interplanar d value of exactly 3.35 Å and a long-range crystalline order with crystallite size of at least a few dozen nanometers (Luque et al., 1998). The chemical bonds within the layers of hexagonally arranged carbon atoms are covalent with sp^2 hybridization (Fitzer et al., 1995; Langenhorst and Campione, 2019). The thermodynamic properties of carbon without long-range crystalline order and of poorly crystallized and/or defect-rich ("disordered") graphitic carbon are not available at high-pressure and high-temperature conditions, hence thermodynamic models generally assume perfect ordering and well-developed crystallinity of graphite. Although some studies suggested that "disordered" graphite and well-crystallized graphite may display different dissolution behavior in aqueous fluids (Ziegenbein and Johannes, 1980; Connolly, 1995; Luque et al., 1998), others concluded that their thermodynamic properties must be very similar (McCollom, 2013).

In this study, we provide the first experimental results on the high-pressure/high-temperature dissolution at relatively oxidized conditions of (i) ordered crystalline graphite (with crystallite size around 50 nm determined by synchrotron X-ray diffraction and small Raman "disorder" D peak) and (ii) X-ray amorphous glass-like carbon, by measuring the CO_2 content of aqueous fluids in equilibrium with these two sp^2-hybridized carbon forms. Glass-like carbon is indeed a typical disordered sp^2 bonded carbon (like graphitic carbon) consisting of randomly distributed curved graphene layer (also called disordered multilayer graphene, or DMLG) fragments dispersed in an amorphous matrix (Hu et al., 2017). Glass-like carbon is non-crystalline (X-ray amorphous) and non-graphitizing, meaning that it resists the development of graphite crystals up to 3000 °C at room pressure, and up to 45GPa at room temperature (Shiell et al., 2018). From a thermodynamic point of view, glass-like carbon can be considered as a quasi-amorphous or crypto-crystalline solid with crystallite dimensions smaller than 5–8 nm (Guencheva et al., 2001). In light of these properties, we used glass-like carbon as an analogue of poorly organized organic matter. The advantage of using glass-like carbon instead of other poorly crystalline disordered carbon allotropes lies in its metastable persistence at the investigated experimental conditions (1–3GPa, 800 °C, 12–24 h). Other disordered carbon materials, such as saccharose-based char, are known to recrystallize promptly at high-pressure/high-temperature conditions (Beyssac et al., 2003), which would prevent equilibration between fluids and solid carbon in days-long runs, and therefore the retrieval of thermodynamic parameters. The choice of using glass-like carbon as an analogue for natural disordered carbon is also supported by comparison of

glass-like carbon with char produced by thermal decomposition of glucose at the same experimental conditions.

The experimental results allowed retrieving the difference in Gibbs free energy (G) of glass-like carbon compared to that of crystalline graphite at high pressures and temperatures, demonstrating that, although small, this difference can lead to substantial changes in dissolved carbon content predicted by available thermodynamic models that assume a perfectly ordered crystalline state of graphitic carbon.

2. METHODS

In this study, we use the recommended terminology of IUPAC (Fitzer et al., 1995) for the description of carbon as a solid, which is summarized in the Appendix.

2.1. Bulk compositions, starting materials and buffering strategy

Fluids in equilibrium with crystalline and disordered sp^2 carbon were generated starting from oxalic acid dihydrate (OAD; $H_2C_2O_4 \cdot 2H_2O$; Sigma-Aldrich), highly ordered graphite powder (from spectroscopic-pure rods, gently hand-ground in boron carbide mortar) and glass-like carbon spherical powder (Alfa Aesar; type I, i.e., produced by firing polymeric precursors at temperatures below 2000 °C). Crystalline graphite and glass-like carbon were characterized by scanning-electron microscopy, micro-Raman spectroscopy and synchrotron X-ray diffraction. Additionally, two experiments have been replicated using pure water (MilliQ, boiled while flushed with N_2 to remove dissolved atmospheric CO_2) instead of OAD to check for possible discrepancies. Experiments were buffered using the double-capsule technique (Eugster and Skippen, 1967) to prevent the direct contact with the buffering assemblages, with an inner H_2-permeable $Au_{60}Pd_{40}$ capsule (OD = 2.3 mm) and an outer Au capsule (OD = 4.5 mm). The outer capsule contained H_2O and either the fayalite–magnetite–quartz (FMQ) or the nickel–nickel oxide (NNO) buffers (Fig. 1). Fayalite and magnetite have been synthesized at 1100 °C in a gas-mixing furnace under reducing atmosphere (CO_2: CO = 10:1), starting from stoichiometrically weighted reagent-grade Fe_2O_3 (Sigma-Aldrich) and amorphous SiO_2 from hydrolyzed tetraethyl orthosilicate (Sigma-Aldrich). Natural hyaline quartz powder has been used to build up the final FMQ buffering assemblage. NNO buffer was prepared by mixing Ni metal powder (Sigma-Aldrich) and green NiO nanopowder (Sigma-Aldrich), previously sintered at 1300 °C for 24 h under oxidizing atmosphere to prevent grain size-induced discrepancies with the accepted free-energy values of the NNO buffer (Mattioli and Wood, 1988; O'Neill and Pownceby, 1993). At equilibrium conditions, as long as all the buffering phases are present, the chemical potential of hydrogen is expected to be homogeneous in the inner and in the outer capsules. In the outer capsule, the hydrogen fugacity (fH_2) is constrained through the reactions:
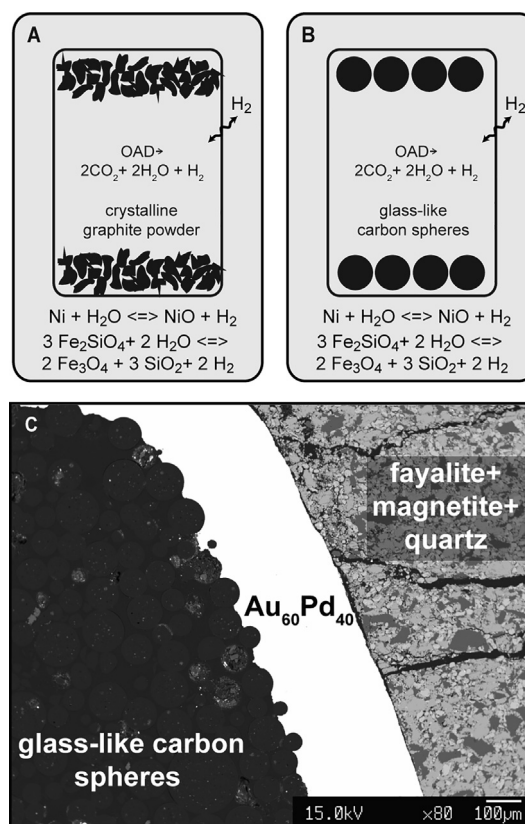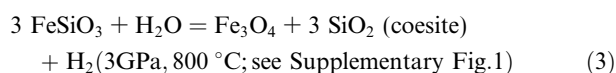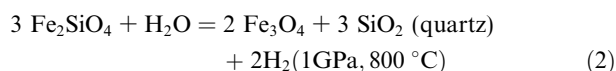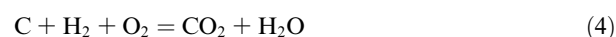
$$Ni + H_2O = NiO + H_2 \quad (1)$$

Fig. 1. Experimental setup. (A, B): sketch of the double capsule system. The inner Au–Pd capsule, permeable to H_2, contains oxalic acid dihydrate (OAD), which decomposes at $T > 200$ °C to CO_2, H_2O and H_2, and either crystalline graphite (A) of glass-like carbon (B). The outer Au capsule contains the inner capsule and the fH_2 buffer, either fayalite-magnetite-quartz-H_2O or nickel-nickel oxide-H_2O. The fH_2 constrained by the buffer is expected to be homogenous in the inner and in the outer capsule. (C): back-scattered electron image of the representative sample COH62 ($P = 1$ GPa and $T = 800$ °C) across the inner Au–Pd capsule boundary, showing glass-like carbon spheres on the left and the fayalite-magnetite-quartz buffer on the right.

$$3\ Fe_2SiO_4 + H_2O = 2\ Fe_3O_4 + 3\ SiO_2 \text{ (quartz)}$$
$$+ 2H_2 (1\,GPa, 800\,°C) \quad (2)$$

$$3\ FeSiO_3 + H_2O = Fe_3O_4 + 3\ SiO_2 \text{ (coesite)}$$
$$+ H_2 (3\,GPa, 800\,°C; \text{see Supplementary Fig.1)} \quad (3)$$

In the inner capsule, the equilibration of the COH fluid is accomplished by the fH_2-dependent coupled reactions (Tumiati et al., 2017):

$$C + H_2 + O_2 = CO_2 + H_2O \quad (4)$$

and

$$C + 2\ H_2O = CO_2 + 2\ H_2 \quad (5)$$

As a consequence, the initial fluid composition (H_2O: CO_2 = 1:1 starting from OAD) adjusts its CO_2 fraction until equilibrium in fH_2 is reached between the inner and

the outer capsule. The oxygen fugacity (fO_2) in the inner capsule (containing mixed H_2O–CO_2 fluids instead of pure water) is constrained indirectly and it will be slightly lower compared to the fO_2 constrained in the outer capsule (containing pure H_2O) by FMQ and NNO (cf. Luth, 1989) and it is calculated by thermodynamic modeling (see Section 2.5 and Table 2), ranging from ΔFMQ ($=\log fO_2^{sample} - \log fO_2^{FMQ}$) −0.5 to −0.8.

High-pressure pyrolysis of glucose to char has been conducted in unbuffered single Au capsules (OD = 3 mm) welded shut after filling with anhydrous glucose ($C_6H_{12}O_6$, or CH_2O) produced by dehydration at 70 °C (2 h) of α-D-glucose monohydrate (Sigma Aldrich) (Ponschke and House, 2011).

2.2. Experimental conditions and apparatus

Experiments were performed at 1 and 3 GPa at 800 °C using an end-loaded piston-cylinder apparatus. Capsules were embedded in MgO rods (Norton Ceramics) and inserted in graphite furnaces surrounded by NaCl and borosilicate glass (Pyrex). At the top of the assembly, a pyrophyllite–steel plug was placed to ensure the electrical contact. Temperatures were measured with K-type thermocouples and are considered accurate to ±5 °C. An alumina disk was placed at the top of the capsule to avoid the direct contact with the thermocouple. Pressure calibration of the apparatus is based on the quartz to coesite transition according to Bose and Ganguly (1995) (accuracy ±0.01 GPa). Samples were first pressurized at run pressure, then heated to $T = 800$ °C, with a ramp of 100 °C/min. Experiments were quenched by turning off the power supply, resulting in a rate of temperature decline of >40 °C/sec. The double capsules were prepared by peeling off the outer capsule, then heated at 110 °C in a vacuum oven (>2h) to remove any residual water trapped in the buffer. After the analysis of volatiles (see below), double capsules were mounted in epoxy resin and polished for scanning electron microscopy and micro-Raman spectroscopy. The persistence of the buffering assemblages was always verified by means of electron microprobe analyses. Single capsules containing char derived from the decomposition of anhydrous glucose were analyzed for volatiles, then opened to collect the sample, which has been analyzed by scanning electron microscopy, micro-Raman spectroscopy and synchrotron X-ray diffraction.

2.3. Analysis of solids

Solid carbon in both buffered and unbuffered runs has been characterized by scanning electron microscopy, micro-Raman spectroscopy and synchrotron X-ray diffraction. Graphite and glass-like carbon were analyzed both as starting materials and after quench from run P–T conditions.

Quantitative analyses and back-scattered electron imaging of the experimental products were performed to check the integrity of the buffering mineral assemblages, using a JEOL 8200 wavelength-dispersive (WDS) electron microprobe, at 15 kV accelerating potential, 5 nA sample current

and 1 μm beam size. Standards used were fayalite (Fe), niccolite (Ni) and grossular (Si). A counting time of 30 s (10 s background) was used for all the elements. Secondary electron imaging of pyrolytic carbon has been performed at 15 kV and 0.05 nA sample current.

Micro-Raman spectra were acquired using the integrated micro/macro-Raman LABRAM HRVIS (Horiba Jobin Yvon Instruments) of the Interdepartmental Center "G. Scansetti" (Department of Earth Sciences, University of Torino, Italy). Excitation lines at 532 nm (solid-state Nd laser and 80 mW of emission power) were used with Edge filter and a grating of 600 grooves/mm. Calibration was performed using the 520.6 cm^{-1} Si band. The laser power on the sample was set upon the measured materials at 2mW by the addition of filters. Acquisition times were set at 25 s for 3 accumulations with a laser spot of 2 μm.

X-ray Powder diffraction (XRD) data were obtained at XRD1 beamline (Elettra, Trieste, Italy). The samples were placed in glass capillaries and mounted onto the head of the Huber Kappa Goniometer installed at the beamline. The data were collected with a monochromatic radiation ($\lambda = 0.7000$ Å), using a Dectris Pilatus 2 M detector. The beam size at the sample was of 0.2×0.7 mm and the calibration of the set-up geometry was checked with a LaB$_6$ pattern. Successively, the images were integrated with Fit2D software package (Hammersley et al., 1995; Hammersley, 1997) and analyzed using the GSAS EXPGUI software (Toby, 2001).

2.4. Analysis of volatiles

For the analysis of quenched volatiles in the capsules (Table 1) we employed the capsule-piercing technique (Tiraboschi et al., 2016). Volatiles, heated to $T \approx 80$ °C to allow liquid water to be converted into water vapor, were extracted from the capsules in a Teflon reactor and conveyed to a quadrupole mass spectrometer (EXXTORR 0–200 amu, Mod. XT 200, equipped with secondary electron multiplier) using ultrapure Ar as carrier gas. The pressure conditions in the reactor were monitored through high-resolution sensor gauges (±1 mbar precision). The temperature in the reactor was monitored with K-type thermocouple. Gas mixtures of known compositions and ultrapure water were utilized for the calibration of the quadrupole mass spectrometer. The technique enabled the retrieval of micromolar quantities of the volatiles H_2O, CO_2, CO, CH_4, H_2 and O_2 with uncertainties of ~1 mol% (10 mol% for CO, due to the interference with atmospheric N_2 on the 28 m/z channel). The periodic analysis of test capsules filled with 1 mg of oxalic acid dihydrate, thermally decomposed at 250 °C to H_2O, CO, CO_2 and H_2 (Tiraboschi et al., 2016), ensures the stability and the reproducibility of the analyses over time.

2.5. Thermodynamic modeling

The volatile composition of carbon-saturated COH fluids, and in particular their XCO_2 [$=CO_2/(H_2O + CO_2)_{molar}$] in relatively oxidized systems, is dependent on the redox state of the system (cf. the review of Tumiati and

Table 1
Run table of the experiments and volatiles measured using the capsule-piercing technique.

Run	P (GPa)	T (°C)	capsule	buffer	runtime (h)	starting materials	total volatiles (µmol)	H$_2$O	CO$_2$	CO	CH$_4$	H$_2$	XCO$_2$
COH69	1	800	double	FMQ	88	OAD + graphite	8.14	2.40(6)	4.98(3)	0.00(60)	0.02(5)	0.00(1)	0.674(7)
COH70	1	800	double	NNO	92	OAD + graphite	7.21	1.80(6)	4.87(3)	0.00(59)	0.02(5)	0.02(1)	0.731(8)
COH76	3	800	double	FMQ	48	OAD + graphite	5.51	1.19(2)	3.43(1)	0.03(24)	0.00(2)	0.000(5)	0.74(2)
COH105	3	800	double	FMQ	24	H$_2$O + graphite	11.2	2.51(5)	6.28(2)	0.76(39)	0.04(3)	0.00(1)	0.714(5)
COH103	3	800	double	NNO	24	OAD + graphite	49.5	47.1(2)	4.86(8)	0.5(1.5)	0.02(13)	0.00(3)	0.094(1)
COH62	1	800	double	FMQ	24	OAD + glass-like carbon	7.34	1.21(6)	4.84(3)	0.00(64)	0.01(6)	0.00(1)	0.801(9)
COH57	1	800	double	NNO	24	OAD + glass-like carbon	6.88	0.89(4)	5.03(2)	0.00(42)	0.02(4)	0.00(1)	0.850(6)
COH112	3	800	double	FMQ	24	OAD + glass-like carbon	8.73	2.93(11)	3.84(5)	0.07(93)	0.02(8)	0.00(2)	0.57(1)
COH108	3	800	double	FMQ	24	H$_2$O + glass-like carbon	8.31	2.59(21)	2.59(9)	0(2)	0.09(14)	0.00	0.50(3)
COH100	3	800	double	NNO	24	OAD + glass-like carbon	20.7	15.83(2)	1.74(1)	0.06(19)	0.02(02)	0.334(4)	0.099(1)
COH122	1	800	single	-	12	glucose anhydrous	23.31	14.27(1)	1.10(1)	0.58(11)	5.04(2)	0.005(4)	0.072(1)
COH124	1	800	single	-	24	glucose anhydrous	52.40	38.8(2)	12.3(1)	0(1)	2.3(2)	0.00(6)	0.240(3)
COH123	3	800	single	-	24	glucose anhydrous	60.74	48.16(1)	0.48(1)	0.48(5)	0.05(1)	0.000(2)	0.0098(3)

Standard deviation (2 sigma) expressed in bracket notation.
FMQ: fayalite-magnetite-quartz-H$_2$O (ferrosilite-magnetite-coesite-H$_2$O at 3GPa, 800 °C).
NNO: nickel-nickel oxide-H$_2$O.
OAD: oxalic acid dihydrate.
XCO$_2$ = CO$_2$/(H$_2$O + CO$_2$)$_{molar}$.

Malaspina, 2019), which can be controlled indirectly in experiments by fixing the hydrogen fugacity in double capsules (e.g., Eugster and Skippen, 1967).

The fugacities of oxygen and hydrogen in the outer and in the inner capsules at NNO and FMQ conditions were calculated using the Perple_X package (Connolly, 2005), using the thermodynamic dataset of Holland and Powell (Holland and Powell, 1998) revised by the authors in 2004 (hp04ver.dat), the Perple_X water equation of state (EoS) "H–O HSMRK/MRK hybrid", and using the Excel spreadsheet GFluid (Zhang and Duan, 2010) with the COH fluid EoS of Zhang and Duan (2009), which is based on the equilibrium constants K_p of the following reactions:

$$C + O_2 = CO_2 \tag{6}$$

$$C + 0.5\ O_2 = CO \tag{7}$$

$$H_2 + 0.5\ O_2 = H_2O \tag{8}$$

$$C + 2\ H_2 = CH_4 \tag{9}$$

Tumiati et al. (2017) showed that the composition of graphite-saturated COH fluids at 1–3GPa and 800 °C are reproduced best using a modified version of Zhang and Duan's model, implemented with fH$_2$ coefficients (γH$_2$) changing dynamically as a function of X(O) [$=O_2/(H_2 + O_2)_{molar}$], taken from the EoS of Connolly and Cesare (1993). Therefore, in this study we refer to this modified model to: (i) predict the composition of buffered fluids in equilibrium with crystalline graphite (Table 2); (ii) compare it with the measured composition of fluids in equilibrium with either crystalline graphite or glass-like carbon (Fig. 2; Table 1) and (iii) retrieve the difference in free energy between graphite and glass-like carbon (ΔG), by iteratively changing the Zhang and Duan's K_ps (cf. Eqs. (4)–(7)) to account for the measured XCO$_2$ of fluids in equilibrium with the latter phase (Table 3). The experimental ΔG was compared with the ΔG predicted by thermodynamic modeling, performed with thermodynamic parameters retrieved from literature added to the database of Holland and Powell (hp04ver.dat) (Table 4), thus making feasible with Perple_X the calculation of G–P and log fO$_2$–(P, T) phase diagrams involving glass-like carbon in addition to crystalline graphite.

Recent studies highlight the importance of non-volatile charged carbon species (not detectable with the capsule-piercing technique) and/or organic dissolved compounds in high-pressure COH fluids at certain P–T–fO$_2$–pH conditions (Sverjensky et al., 2014a,b; Pan and Galli, 2016; Tiraboschi et al., 2018; Huang and Sverjensky, 2019). In particular, Sverjensky et al. (2014b) showed that at high pH values aqueous bicarbonate and carbonate species become dominant instead of molecular CO$_2$ and CH$_4$. In addition, organic dissolved species (e.g., formates and acetates) may form at ultra-high pressures (e.g., 5GPa at 600 °C in Sverjensky et al., 2014b). Therefore, conventional thermodynamic models (Connolly and Cesare, 1993; Zhang and Duan, 2009), which consider neutral molecular species only, are not always adequate to predict carbon speciation in subduction fluids. It is an open question whether the available thermodynamic models are still valid in the

Table 2
Thermodynamic modelling of graphite-saturated fluids buffered at the investigated P–T–fH_2 conditions.

P (GPa), T (°C)	1, 800	1, 800	3, 800	3, 800
buffer	NNO	FMQ	NNO	FMQ
log fO_2 outer capsule[a]	−13.47	−13.70	−12.62	−11.19
log fH_2 outer capsule = inner capsule[b]	1.775	1.889	3.107	2.361
Modeled composition at fixed fH_2 (mol%)[c]				
H_2O	28.74	34.25	65.34	26.60
CO_2	70.46	64.93	34.59	73.33
CO	0.66	0.64	0.05	0.07
CH_4	0.06	0.09	0.02	0.00
H_2	0.08	0.09	0.01	0.00
XCO_2[d]	0.710	0.655	0.346	0.733
XO[e] inner capsule	0.746	0.705	0.507	0.765
log fO_2 inner capsule	−14.28	−14.31	−11.99	−11.66
ΔFMQ[f] inner capsule	−0.58	−0.61	−0.80	−0.47
pH[g]	3.25	3.26	2.34	2.22

[a] retrieved using the Perple_X package and the hp02ver.dat database (see also Supplementary Fig. 4), considering the reactions: i) 2 Ni + O_2 = 2 NiO; ii) 3 Fe_2SiO_4 + O_2 = 2 Fe_3O_4 + 3 SiO_2 (1GPa–800 °C; quartz stable) and iii) $3FeSiO_3$ + O_2 = Fe_3O_4 + 3 SiO_2 (3GPa–800 °C; coesite stable).

[b] retrieved using the routine "fluids" of the Perple_X package (H-O HSMRK/MRK hybrid EoS).

[c] EoS by Zhang and Duan (2009) with dynamic γH_2 taken from Connolly and Cesare (1993), changing as a function of P, T and XO (γH_2 = A × $(XO)^3$ + B × $(XO)^2$ + C × XO + D; where A = 43.919, B = 114.55, C = −105.75, D = 41.215 at 1GPa–800 °C; A = -11208; B = 26723, C = -21949, D = 6979.2 at 3GPa–800 °C).

[d] XCO_2 = CO_2 / $(H_2O + CO_2)_{molar}$

[e] XO = O_2 / $(H_2 + O_2)_{molar}$

[f] ΔFMQ = log fO_2 − log fO_2^{FMQ}

[g] retrieved using the Deep Earth Water model by fixing the fO_2 of the inner capsule; neutral pH at 1GPa–800 °C = 4.02; neutral pH at 3GPa–800 °C = 3.09.

presence of COH fluid immiscibility, suggested at P = 1.5–2.5GPa and T = 600–700 °C in graphite-saturated slightly saline fluids (Li, 2016) and in low-temperature/high-pressure hydrocarbon fluids (Huang et al., 2017). In particular, Li (2016) found at 2.5GPa and 700 °C at Re–ReO$_2$ redox conditions ($\approx\Delta FMQ$ = +2) mixed H_2O–CO_2 fluids in equilibrium with almost pure CO_2. As the capsule-piercing technique used in our study only allows measurement of the bulk volatile components, it cannot be used to investigate fluid immiscibility. However, on the basis of the results given in our study and in previous works (Matveev et al., 1997; Tiraboschi et al., 2016; Tumiati et al., 2017), the conventional models are still able to predict the *bulk* composition (but not necessarily the speciation) of high-pressure fluids in terms of bulk CO_2/$(H_2O + CO_2)$ and CH_4/$(H_2O + CH_4)$, although they could fail at certain P–T–fO_2–pH conditions where species other than H_2O, $CO_{2(aq)}$ and $CH_{4(aq)}$ become dominant. In order to justify our experimental approach we used the Deep Earth Water thermodynamic model (Sverjensky et al., 2014a) to confirm that molecular $CO_{2(aq)}$ is by far the dominant carbon-bearing fluid species at our experimental conditions, and to estimate the pH of the fluids (Table 2).

3. RESULTS

3.1. Characterization of solid carbon

3.1.1. Crystalline graphite

Back-scattered electron observation of graphite powder used as starting material did not reveal any foreign material.

The powder consists of homogeneous flakes with grain size of 10–100 μm (Supplementary Fig. 2a). X-ray powder diffraction showed that the powder is monomineralic and crystalline, with a sharp diffraction peak at d_{002} = 3.3672 Å (Supplementary Fig. 3 – graphite). The fitted pattern showed that the averaged crystallite size of the sample is around 50 nm. Micro-Raman spectroscopy of unpolished graphite powder showed a sharp graphite (G) peak at 1600 cm^{-1} and only a little disorder (D) peak at 1350 cm^{-1}, confirming that this material is highly ordered (Ferrari, 2007) (Supplementary Fig. 4). The G' peak (also called 2D in Ferrari, 2007) at about 2700 cm^{-1} is also well developed. Raman spectra of polished graphite showed a marked increase of the D peak owing to mechanical modifications during the polishing (Pasteris, 1989), and was therefore not considered. Quenched graphite samples did not show any evidence of substantial modification with respect to starting graphite powder, within the uncertainties caused by polishing.

3.1.2. Glass-like carbon

Glass-like carbon spheres used as starting material appeared homogenous at the scanning electron microscope. They are about 100 μm in size, and show sparse closed porosity (Supplementary Fig. 2b). X-ray powder diffraction of the spherical powder showed broad peaks, typical of amorphous materials (Supplementary Fig. 3). Micro-Raman spectra show broad G and D peaks, which characterize amorphous sp^2 carbon (cf. Ferrari and Robertson, 2001), with D peak > G peak (Fig. 2). The G' peak is poorly developed. Glass-like carbon retrieved after runs showed Raman spectra identical to the starting material.
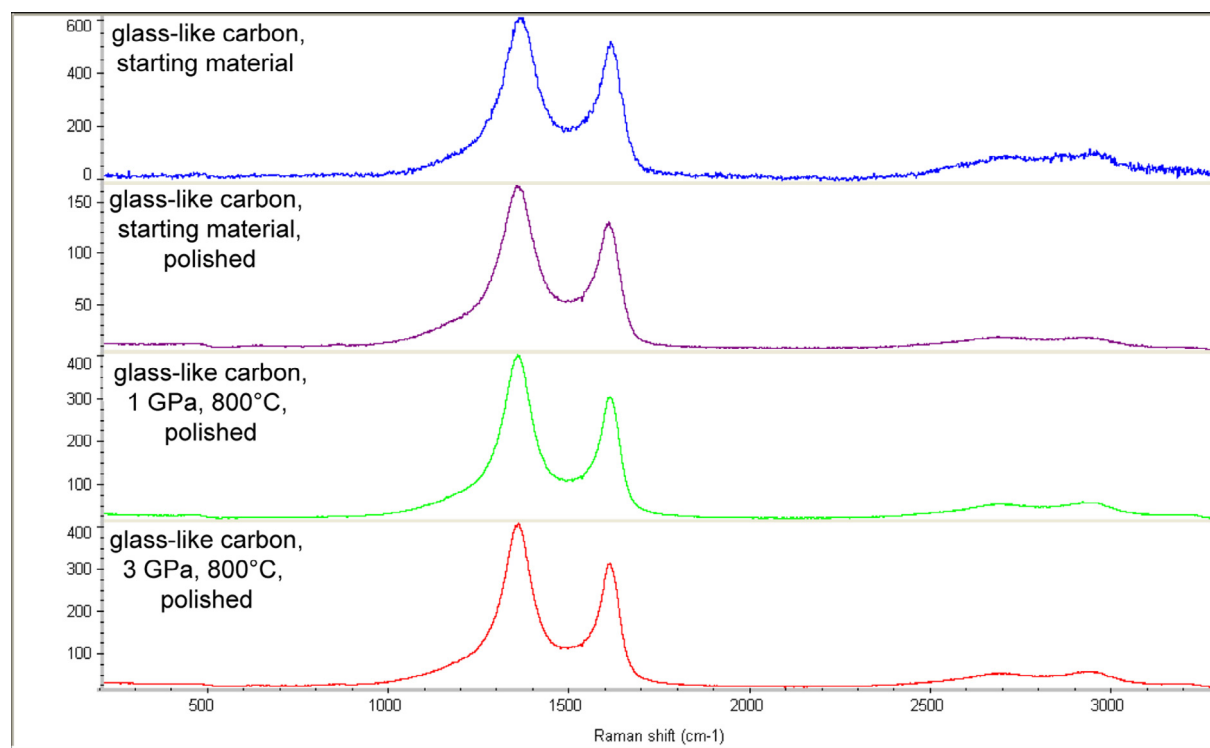
Fig. 2. Micro-Raman spectra of glass-like carbon as starting material (unpolished: blue; polished: purple) and as quenched product from 1GPa–800 °C (green) and from 3GPa–800 °C (red). (For interpretation of the references to colour in this figure legend, the reader is referred to the web version of this article.)

Table 3
Equilibrium constants (K_p) at $T = 800$ °C and difference in Gibbs free energy of glass-like carbon with respect to crystalline graphite (ΔG), retrieved from measured fluid composition.

Carbon form	graphite	glass-like carbon	glass-like carbon	graphite	glass-like carbon	glass-like carbon
Pressure GPa	1	1	1	3	3	3
Buffer	-	NNO	FMQ	-	NNO	FMQ
log K_p C + O$_2$ = CO$_2$	44.98[a]	45.16[b]	45.17[b]	46.12[a]	46.18[b]	45.86[b]
log K_p C + 0.5 O$_2$ = CO	23.77[a]	23.95[b]	23.96[b]	24.91[a]	24.97[b]	24.65[b]
log K_p C + 2 H$_2$ = CH$_4$	−2.48[a]	−2.30[b]	−2.29[b]	−1.33[a]	−12.7 [b]	−1.59[b]
ΔG (kJ mol^{-1})[c]	-	1.6(1)	1.7(1)	-	0.51(1)	−2.3(2)

[a] EoS by Zhang and Duan (2009) (GFluid), at $T = 800$ °C.
[b] calculated by simulation analysis to fit measured XCO_2 (=CO_2/H_2O + CO_2) of samples COH57, COH62, COH100 and COH112, assuming constant fH_2.
[c] $\Delta G = G_{\text{glass-like C}} - G_{\text{graphite}}$ at $T = 800$ °C, calculated using the equation: $\Delta G = RT \times \ln (K_p^{\text{glass-like C}}/K_p^{\text{graphite}})$; the uncertainty in ΔG (bracket notation) has been calculated taking into account the standard deviation of QMS analyses (Table 1).

3.1.3. Char from high-pressure pyrolysis of anhydrous glucose

Secondary electron imaging of solid carbon formed by decomposition of glucose (char) at 1–3GPa and 800 °C show microtextures that are dependent on the run duration. In the 12-h run at 1GPa, char comes as a loose spherical powder with an average grain size of 1 μm (Fig. 3a, b). In the 24-h runs at 1 and 3GPa, spherical elements are not visible, and char is characterized by a glass-like appearance with conchoidal fracture and absence of cleavage (Fig. 3c–f). X-ray powder diffractions of char (Supplementary Fig. 3) show that the diffraction angle of the most

intense peak is lower compared to that of crystalline graphite, while the full width at half maximum (FWHM) is higher, meaning a decline of the crystallite size. The crystallite size of char synthesized at the investigated high-pressure conditions is of about 2–4 nm typical of nano-crystalline materials. The Raman spectra of char synthesized at 1 and 3GPa in 24-h long runs are very similar, with broad G and D peaks ($D > G$) (Fig. 4). Compared to glass-like carbon, the D peak is slightly higher, but broadening of the peaks is a little less pronounced. The G' peak is comparable to that of glass-like carbon. The Raman spectrum of char synthesized at 1GPa in the shorter 12-h run is characterized
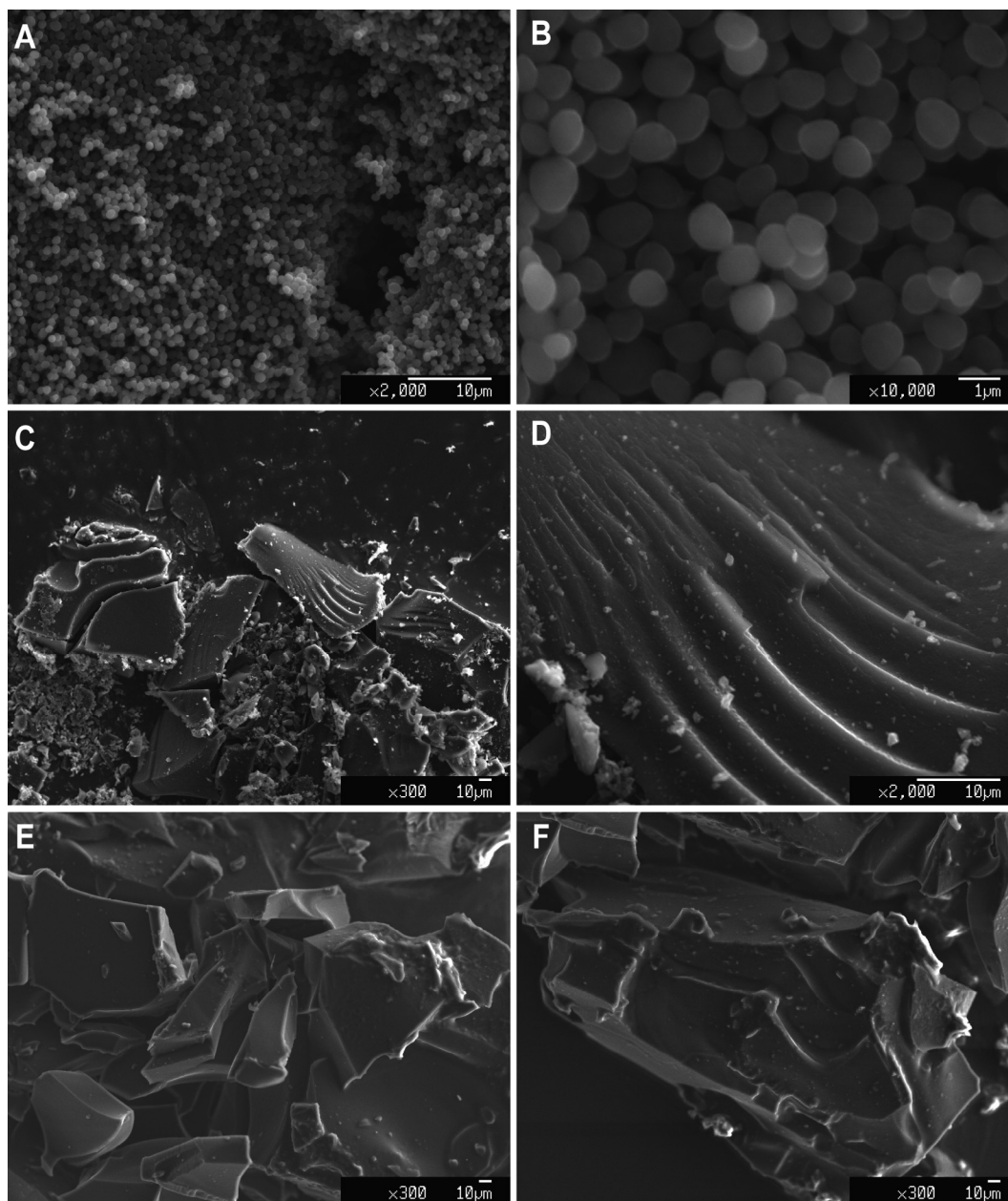
Fig. 3. Secondary electron images of char synthesized from glucose at 800 °C and high-pressure conditions. (A, B): $P = 1$GPa, runtime 12 h; (C, D): $P = 1$GPa, runtime 24 h; (E, F): $P = 3$GPa, runtime 24 h.

by similar G and D peaks, but remarkably higher G' peak (Supplementary Fig. 5), which characterizes crystalline graphite (Fig. 4).

3.2. Characterization of the fluid phase

Volatiles in all the experimental runs have been measured by means of the capsule-piercing technique (see details in Tiraboschi et al., 2016) (Table 1; Fig. 5; Supplementary Fig. 6). Total measured volatiles range from 5.51 to 49.5 micromoles in double capsules where fluids were interacting with either crystalline graphite or glass-like car-

bon, and from 23.21 to 60.74 micromoles in single capsules where fluids were produced by complete dehydration of anhydrous glucose due to the reaction:

$$CH_2O = C + H_2O \qquad (10)$$

3.2.1. Buffered COH fluids interacting with crystalline graphite

Fluids synthesized at 1–3GPa and 800 °C contain mostly H_2O and CO_2, with only traces of CO, CH_4 and H_2 (typically close to or below the detection limit). At $P = 1$GPa, XCO_2 [$CO_2/(H_2O+CO_2)_{molar}$] ranges from 0.674 ± 0.007
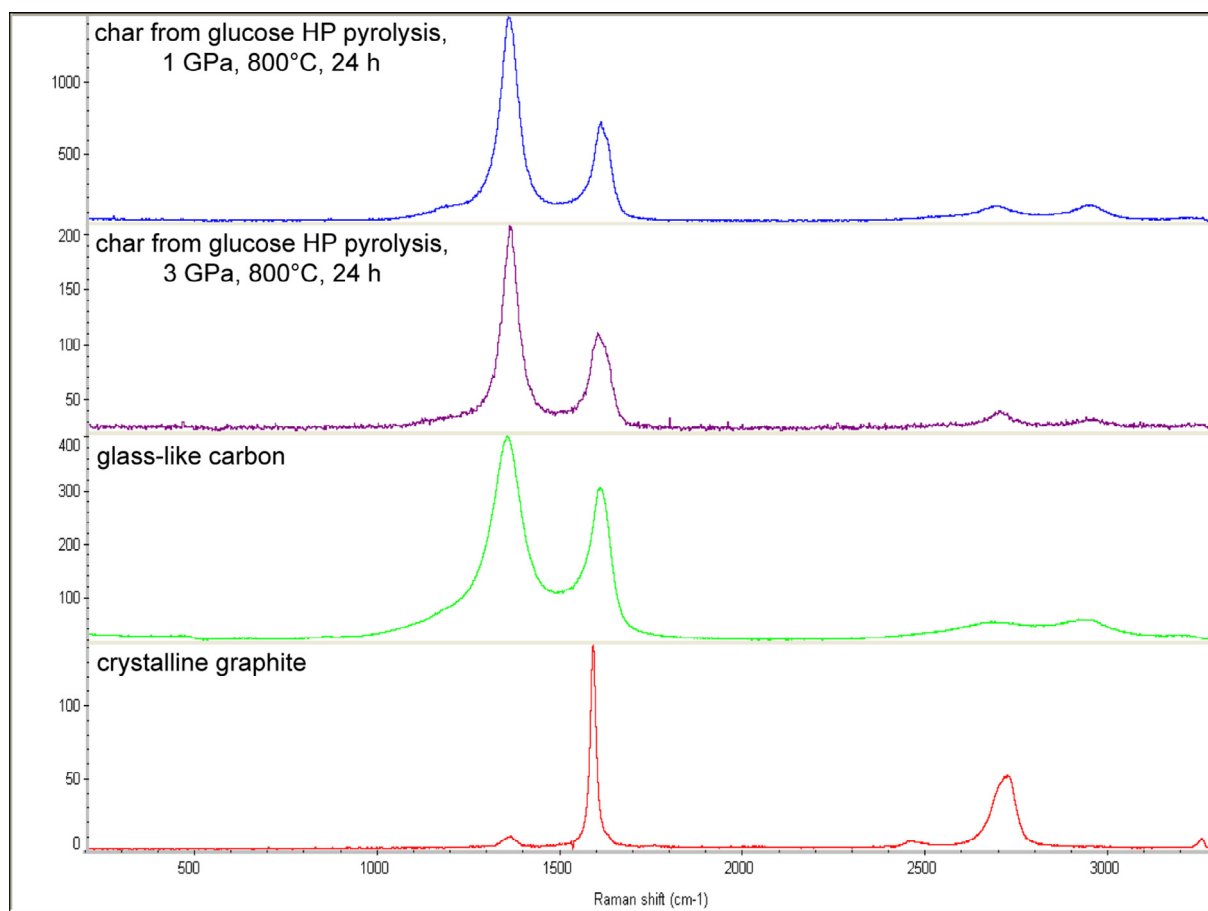
Fig. 4. Raman spectra of quenched char (1GPa: blue; 3GPa: purple) compared with glass-like carbon (green) and crystalline graphite (red). (For interpretation of the references to colour in this figure legend, the reader is referred to the web version of this article.)

(fH_2^{FMQ}) to 0.731 ± 0.008 (fH_2^{NNO}). Because the FMQ and NNO buffers cross at about 1.5GPa (cf. Supplementary Fig. 1), meaning that the NNO buffer is more oxidizing than FMQ at $P < 1.5$GPa and less oxidizing at $P > 1.5$GPa, fluids at $P = 3$GPa buffered by NNO are expected to show lower XCO_2 compared to fluids buffered by FMQ (Table 2). At fH_2^{FMQ}, the run COH76, containing oxalic acid dihydrate (OAD) as starting source of fluid, displays $XCO_2 = 0.74 \pm 0.02$, and run COH105, containing water instead of OAD, displays a similar XCO_2 of 0.714 ± 0.05. Instead, at fH_2^{NNO} conditions the fluid phase is dominated by water, resulting an XCO_2 of 0.094 ± 0.001 in run COH103.

3.2.2. Buffered COH fluids interacting with glass-like carbon

Fluids interacting with glass-like carbon at 1–3GPa and 800 °C, buffered by either FMQ or NNO, contain only traces of CO, CH_4 and H_2, as in the case of graphite-saturated fluids (Table 1). However, the fluids with glass-like carbon display different XCO_2 ratios to the graphite-saturated ones (Fig. 5). In particular, fluids at 1GPa display a higher CO_2 content, and are characterized by XCO_2 of 0.801 ± 0.009 at fH_2^{FMQ} and 0.850 ± 0.006 at fH_2^{NNO}, corresponding to a higher content of +19 and +16 mol% CO_2, respectively, if compared to graphite-

saturated fluids displaying $XCO_2 = 0.674$ at fH_2^{FMQ} and 0.731 at fH_2^{NNO} (see above). However, the higher CO_2 compared with graphite-saturated fluids declines dramatically at 3GPa. At this pressure, fluids saturated with glass-like carbon buffered at fH_2^{NNO} show indeed a XCO_2 of 0.099 ± 0.001, corresponding to only +5 mol% CO_2 higher content relative to fluids saturated with graphite displaying $XCO_2 = 0.094$. Fluids buffered at fH_2^{FMQ} conditions show CO_2 content that is even lower than that characterizing graphite-saturated fluids. In fact, run COH112 is characterized by $XCO_2 = 0.57 \pm 0.01$ (0.50 ± 0.03 in run COH108, with H_2O instead of OAD as starting source of fluid), corresponding to a lower CO_2 content of –24 mol% CO_2 relative to fluids saturated with graphite ($XCO_2 = 0.74$; see above).

3.2.3. Unbuffered COH fluids generated by high-pressure thermal decomposition of glucose

Fluids produced by high-pressure dehydration of anhydrous glucose display variable compositions, changing as a function of run time and pressure conditions (Table 1; Supplementary Fig. 6). Fluids at 1GPa show high contents of CH_4, especially in run COH122 characterized by a relatively short runtime of 12 h. In this run, XCO_2 is 0.072 ± 0.001 and XCH_4 [$=CH_4/(H_2O + CH_4)_{molar}$] = 0.261. Fluid in run COH124, characterized by a longer duration
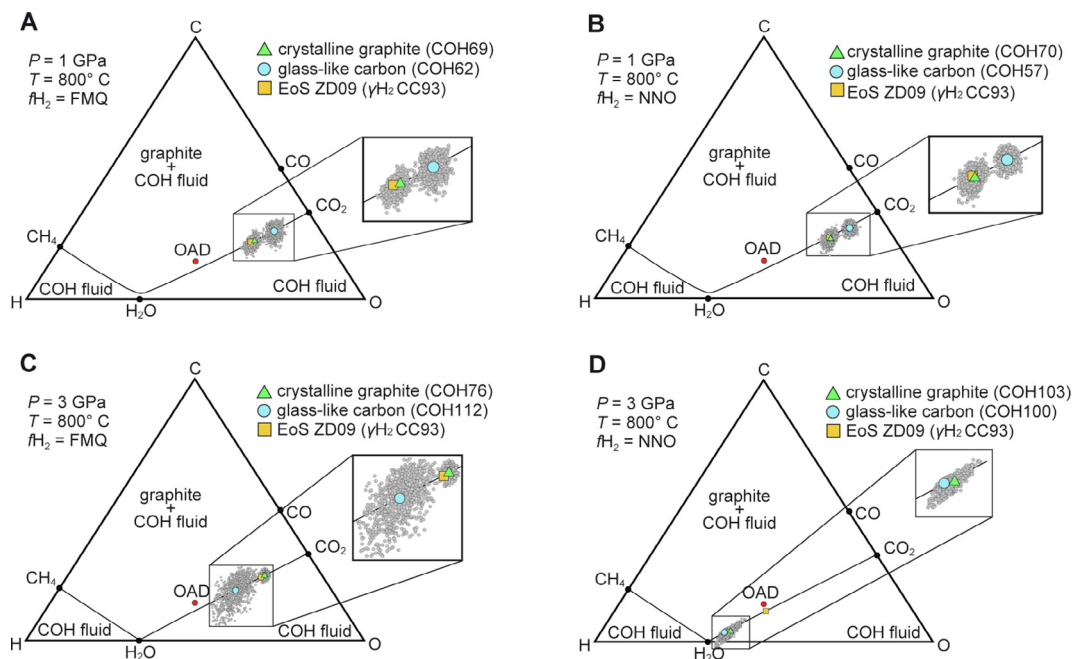
Fig. 5. Fluid compositions at the investigated P–T–fH_2 measured using the capsule-piercing technique (Tiraboschi et al., 2016), plotted on ternary C–O–H diagrams. Red dots: oxalic acid dihydrate (starting fluid composition). Green triangles: fluids in equilibrium with crystalline graphite. Blue dots: fluids in equilibrium with glass-like carbon. Yellow squares: composition of graphite-saturated fluids according to the modified model of Zhang and Duan (2009) (see text for details). Grey dots: analytical uncertainty cloud estimated by Monte Carlo method using the standard deviations provided in Table 1. (For interpretation of the references to colour in this figure legend, the reader is referred to the web version of this article.)

of 24 h, displays a higher XCO_2 of 0.240 ± 0.003 and a lower CH_4 content ($XCH_4 = 0.056$). Fluid at 3GPa (24 h) is nearly pure water with $XCO_2 = 0.0098 \pm 0.0003$ and $XCH_4 = 0.001$.

4. DISCUSSION

4.1. Comparison between experimental results and available thermodynamic models of fluids in equilibrium with crystalline graphite

The measured compositions of COH fluids interacting with crystalline graphite at 1GPa and 800 °C (Table 1) is in excellent agreement, in both FMQ- and NNO-buffered experiments, with the compositions predicted at equilibrium conditions by the modified thermodynamic model of Zhang and Duan (2009) (Table 2; see details of the model in Section 2.5). At 3GPa, while the fH_2^{FMQ}-buffered fluid matches the composition predicted by the model, the measured composition of the fluid buffered externally by NNO is characterized by a lower content of CO_2. The measured XCO_2 would be consistent with an inner-capsule log fO_2 of –12.56, instead of the predicted value of –11.99 (Table 2). At this stage, we can only speculate that this could be ascribed to uncertainties associated to the nickel–nickel oxide buffer (c.f. O'Neill and Pownceby, 1993), which could affect the estimates of fO_2 and fH_2 imposed by the NNO buffer at 3GPa.

Some recent studies underlined the importance of the variable pH in governing the abundance of dissolved

organic species and charges species (e.g., bicarbonates, carbonates) instead of molecular species (Sverjensky et al., 2014b; Pan and Galli, 2016). Therefore, we used the Deep Earth Water (DEW) model (Sverjensky et al., 2014a) to draw pH vs fO_2 diagrams showing the loci of points where graphite is stable in COH fluids at saturation conditions at 1GPa–800 °C (Fig. 6a) and 3GPa–800 °C (Fig. 6b) (black solid lines). The oxygen fugacities expected in COH fluids buffered at fH_2^{FMQ} and fH_2^{NNO} conditions are shown for reference. The intersection of these oxygen fugacities with the graphite-saturation curve represents the investigated experimental conditions (black dots), and thus provides an estimation of the pH value expected in the synthesized fluids, i.e. 3.5–3.6 at 1GPa–800 °C (neutral pH = 4.02) and 2.22 at 3GPa–800 °C (neutral pH = 3.09). The model predicts that at the investigated P–T–fO_2–fH_2 conditions the equilibrium between graphite and COH fluids is thus reached in the $CO_{2(aq)}$ stability field and at acidic conditions, which prevent the stability of carbonate and bicarbonate ions. $CO_{2(aq)}$ is therefore expected to be by far the dominant dissolved carbon-bearing species, while other C–O–H species should occur in very minor amount, the most abundant being ethane ($\approx 10^{-4}$ mol%) at 1GPa–800 °C and formic acid ($\approx 10^{-3}$ mol%) at 3GPa–800 °C. Other organic and/or charged species display even lower abundances. This validates the methodological approach of this study, aiming to retrieve the composition of quenched fluids in terms of volatile molecular species, assuming that they represent the speciation at run conditions. As a corollary, the diagrams in Fig. 6 indicate that when redox conditions are
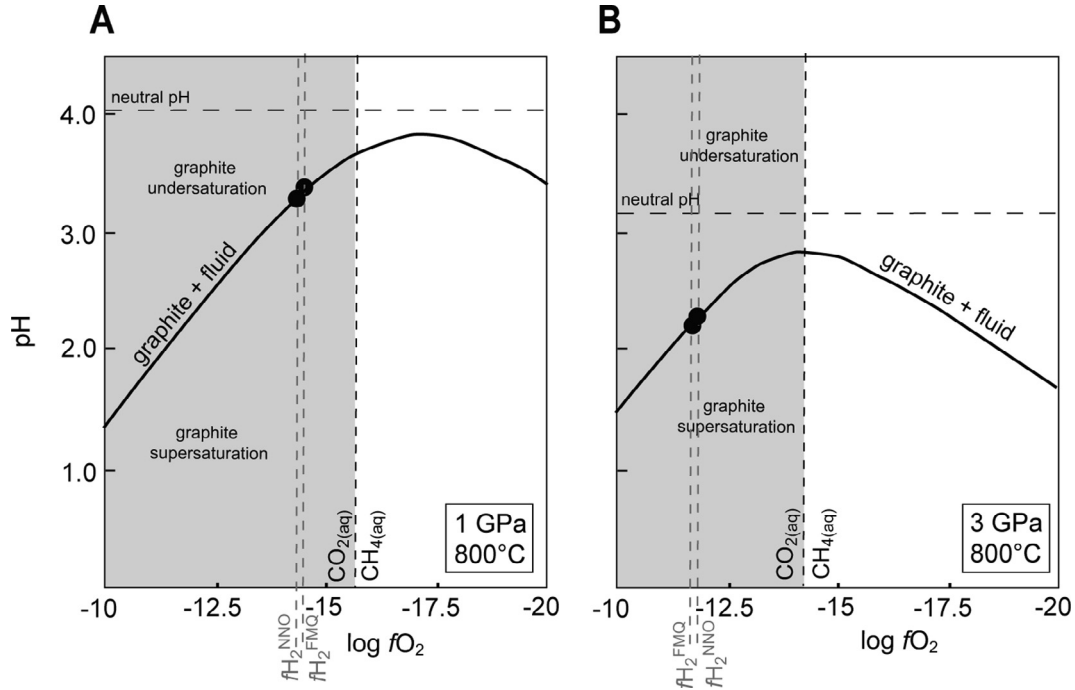
Fig. 6. $\log fO_2$ vs pH diagrams at 1GPa–800 °C (A) and 3GPa–800 °C (B), calculated using the Deep Earth Water model, showing the COH-fluid graphite saturation curve (thick black). Black dots: experimental conditions at fH_2^{FMQ} and fH_2^{NNO}.

imposed on a petrological system (redox-buffered systems), the pH is a dependent variable, as long as graphite-saturation conditions persist. Conversely, in pH-buffered systems, the redox state would be controlled by pH.

4.2. Experimental fluids in equilibrium with glass-like carbon and retrieval of its thermodynamic properties at high-pressure conditions

The CO_2 content of fluids interacting with glass-like carbon is different with respect to the CO_2 content of fluids in equilibrium with crystalline graphite (Fig. 5; Table 1). Fluids at 1GPa are considerably enriched in CO_2, while fluids at 3GPa are only slightly enriched or even depleted with respect to graphite-saturated fluids. The observed difference is $+19$ mol% CO_2 at 1GPa–fH_2^{FMQ}, $+16$ mol% CO_2 at 1GPa–fH_2^{NNO}, $+5$ mol% at 3GPa–fH_2^{NNO} and -24 mol% CO_2 at 3GPa–fH_2^{FMQ}. These different fluid compositions are uniquely ascribable to difference between the thermodynamic properties of glass-like carbon and crystalline graphite. Taking as example Eq. (6) ($C + O_2 = CO_2$), the equilibrium constant of the reaction is:

$$K_p(T) = \frac{[CO_2]}{[O_2]} \tag{11}$$

where brackets indicate equilibrium concentrations of fluid phases over solid carbon.

At 1GPa and 800 °C, involving perfectly crystalline graphite, the equilibrium constant of the reaction following the thermodynamic model of Zhang and Duan (2009) is 3.416×10^{19} (ln $K_p = 44.98$). By changing K_p, the fluid CO_2 content predicted by the model changes accordingly.

By means of iterative calculation, it is possible to find a K_p that fits the measured CO_2 value in runs where fluids reacted with glass-like carbon instead of graphite at the same P–T conditions. The equilibrium constant of a heterogeneous reaction with the participation of glass-like carbon (gl) instead of graphite (graph) can be expressed as:

$$K_{pgl}(T) = K_{pgraph}(T)\exp\left(\frac{\Delta G(T)}{RT}\right) \tag{12}$$

where $\Delta G(T)$ is the difference in Gibbs free energy between glass-like carbon $G_{gl}(T)$ and graphite–$G_{graph}(T)$, and R is the gas constant. This difference can be made explicit, resulting in the equation:

$$\Delta G(T) = RT\ln\left(\frac{K_{pgl}(T)}{K_{pgraph}(T)}\right) \tag{13}$$

As this difference in Gibbs free energy at fixed P–T–fH_2 must be the same for all the reactions (6), (7) and (9), by means of simulation analysis performed with the Solver tool in the Excel spreadsheet provided by Zhang and Duan (2010) we changed iteratively all the pertaining equilibrium constants simultaneously, imposing the mathematical constraint that the resulting ΔG is identical for all the equations, until the model converges to the measured XCO_2. The retrieved ΔG and the equilibrium constants retrieved by simulation analysis at 1 and 3GPa are shown in Table 3. ΔG is almost coincident in runs performed at NNO and FMQ conditions at 1GPa–800 °C, where fluids equilibrated with glass-like carbon contain higher CO_2 fractions compared to graphite-saturated fluids. At these P–T conditions, ΔG is equal to $+1.6(1)$ at fH_2^{NNO} and $+1.7(1)$ kJ/mol at fH_2^{FMQ}. The difference in Gibbs free energy

between graphite and glass-like at 1 GPa agree with previous studies performed at room pressure, where ΔG is +1.8 kJ/mol at 800 °C (Guencheva et al., 2001; Gutzow et al., 2005). At 3 GPa and 800 °C, fluids in equilibrium with glass-like carbon buffered at $f\mathrm{H}_2^{\mathrm{NNO}}$ conditions display a slightly higher CO_2 content compared to graphite-saturated fluids, and ΔG is equal to +0.5(1) kJ/mol. Fluids buffered at $f\mathrm{H}_2^{\mathrm{FMQ}}$ conditions show a CO_2 content which is even lower than fluids in equilibrium with graphite, corresponding to a negative ΔG of –2.3(2) kJ/mol.

4.3. Thermodynamic modeling of glass-like carbon and implications for its stability towards graphite and diamond
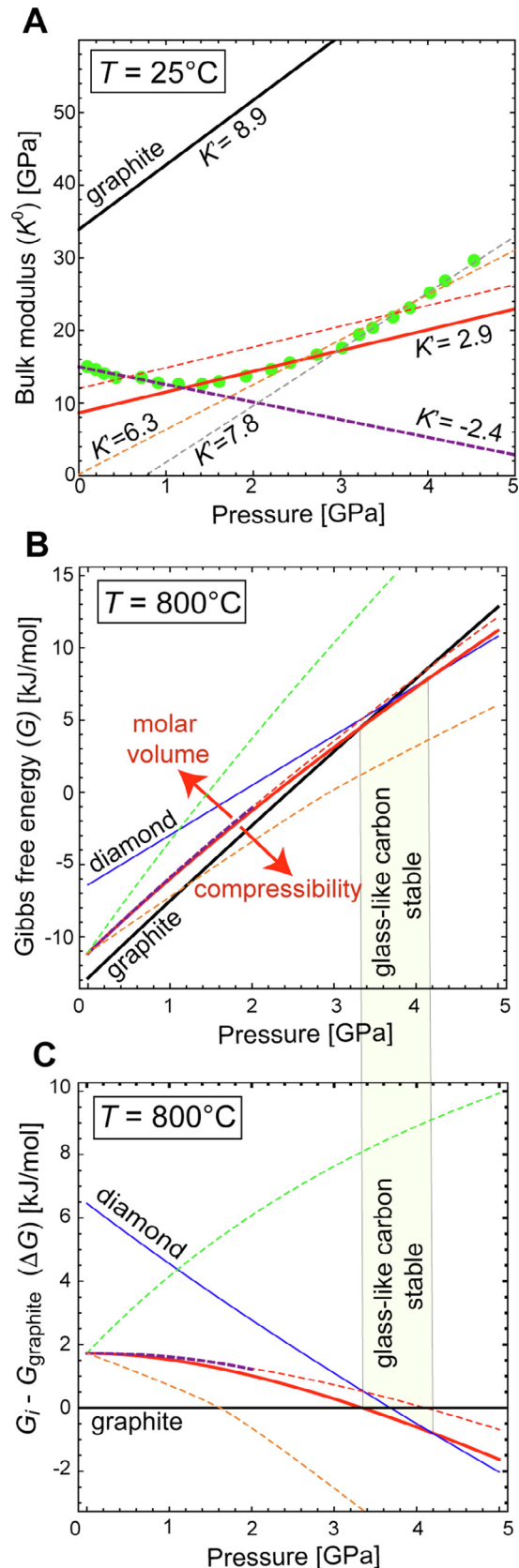
We are not aware of previous Gibbs free energy of glass-like carbon at high pressures, even though layers of glass-like carbon spheres have long been employed in experimental petrology as melt traps at pressure conditions ranging from 1 to 5 GPa (Robinson et al., 1998; Wasylenki, 2003; Dasgupta et al., 2005; Falloon et al., 2008; Spandler et al., 2008). Therefore, we derived the $G(P)$ curve of 5 GPa (Fig. 7), by using the following thermodynamic parameters (Table 4; Supplementary Table 1):

- the standard Gibbs free energy of formation, retrieved from the G–T data of Guencheva et al. (2001) and Gutzow et al. (2005) at room pressure and $T = 298$ K ($\Delta_f G^0 = 2.357$ kJ/mol);
- the standard entropy (S_{298}^0), retrieved by fitting the G–T data at room pressure of Gutzow et al. (2005). The retrieved $S_{298}^0 = 6.6$ J/mol/K agrees well with the standard entropy of 6.2 J/mol/K resulting from the integration of low-temperature heat capacity [$C_P(T)$] measurements (Cappelletti et al., 2018), following:

$$S_{298}^0 = S_0^0 + \int_0^{298} \left[\frac{C_P^0(T)}{T} \right] dT, \qquad (14)$$

taking into account that S_0^0, i.e. the residual entropy at 0 K, is non-zero in amorphous solids;

- the following parameters were assumed to be the same as for graphite (Holland and Powell, 1998; Day, 2012), as they have been reported to be very similar in glass-like carbon: i) the thermal expansion (cf. Cowlard and Lewis, 1967), ii) the coefficients of the heat capacity function (cf. Takahashi and Westrum, 1970; Yokoyama et al., 1971) and iii) the standard molar volume, relying on the fact that the disordered multilayer graphene component in glass-like carbon has a density close to that of graphite (2.25 g/cm³) and the interplanar d-spacings are in broad agreement with those of graphite (Supplementary Fig. 3; cf. also Zhao et al., 2015; Hu et al., 2017). Models with molar volume increased by 50%, reflecting the apparently lower bulk density of

glass-like carbon ($\approx$1.5 g/cm^3; Cowlard and Lewis, 1967; Zhao et al., 2015) imputable to the high closed porosity, are also provided for comparison in Fig. 7b–c.

- the isothermal bulk modulus under standard conditions (K^0) and its first pressure derivative (K') were retrieved by linear regression of the data of type-I glass-like carbon reported by Zhao et al. (2015) (green dots in Fig. 7a), where K^0 is the intercept at 0.0001GPa (1 bar) at 25 °C and K' is the slope of the K–P curves. However, the estimation of glass-like carbon K^0 and K' is not straightforward. Glass-like carbon displays a very high compressibility compared to graphite (cf. bulk modulus data in Day, 2012; Table 4), with a more than halved K^0 decreasing abnormally with increasing pressure up to 1GPa (i.e., negative $K' = -2.4$, corresponding to a K^0 intercept of 15GPa; purple thick dashed lines in Fig. 7), followed by a reversal to positive pressure dependence, accounting to a K' of 2.9 in the 1–3GPa pressure range (extrapolated $K^0 = 9$GPa; red thick lines in Fig. 7; preferred model as it is consistent with the pressures investigated in this study and with K^0 of other forms of non-graphitic sp^2-type carbon; cf. fullerene in Sundqvist and Olabi, 2016) and $K' = 7.8$ at pressures above 3GPa (extrapolated $K^0 = -6$GPa; grey dashed lines in Fig. 7). In Fig. 7b, we show how the choice of different K^0 and K' values affects the $G(P, 800$ °C) of glass-like carbon with pressure increasing from 0 to 5GPa. The predicted difference in Gibbs free energy at 800 °C *versus* pressure between glass-like carbon and graphite (ΔG) using the different models is also shown (Fig. 7c).

At 800 °C, the G–P curves of glass-like carbon (preferred model) and of graphite cross at 3.4GPa, showing a continuous decline of ΔG with increasing pressure, which is 1.5 kJ/mol at 1GPa and 0.29 kJ/mol at 3GPa. These ΔG values match well our experimental results at fH$_2^{NNO}$ conditions (Table 3). Runs buffered at fH$_2^{FMQ}$ conditions agree with the model at 1GPa, while at 3GPa the decline observed experimentally, characterized by a negative ΔG, is more pronounced compared to the model. Models assuming a molar volume coherent with the apparent bulk density of glass-like carbon (1.5 g/cm^3) are inconsistent with experimental results, as they show ΔG values that would increase by increasing pressures (red dashed line in Fig. 7). Negative ΔG values at 3GPa can be reproduced only by models that assume very high compressibility ($K^0 = 2$GPa; orange dashed line in Fig. 7). In this case, however, the intersection point with graphite is shifted at

lower pressures ($\approx$1.5GPa), so that the G–P curve of glass-like carbon would always lie below that of diamond, meaning that, above the intersection point, glass-like carbon would be the stable form of carbon relative graphite and diamond, which is unlikely. On the other hand, the preferred model does intersect the G–P curve of diamond, although it occurs at 4.2GPa, i.e., above the intersection point with graphite at 3.4GPa and above the graphite–diamond transition at 3.7GPa, too. This would imply that in the pressure window 3.4–3.7GPa glass-like carbon could be more stable than graphite and between 3.7 and 4.2GPa it could even be more stable than diamond (yellow field in Fig. 7). However, because of the similar slopes of glass-like carbon- and graphite G–P curves, small fluctuations in the chosen K^0 can result in large uncertainties on the position of the intersection point with graphite relative to the graphite-diamond transition. In fact, a glass-like carbon G–P curve calculated assuming $K^0 = 12$GPa (red dashed lines in Fig. 7) instead of $K^0 = 9$GPa (preferred model) would intersect the G–P curve of diamond at 3.4GPa and the G–P curve of graphite at 4GPa, implying metastability of glass-like carbon at any pressure towards both graphite and diamond, without having a marked effect on the predicted decline of ΔG with increasing pressure.

The estimated thermodynamic parameters of glass-like carbon allow also the calculation of fO$_2$–T phase diagrams at high pressures. In Fig. 8, the boundaries C–CO$_2$ (often referred to as CCO) and enstatite + magnesite = olivine + C (EMOG) are compared considering crystalline graphite and glass-like carbon. At 1GPa, CCO$_{(glass\text{-}like\ carbon)}$ and EMOG$_{(glass\text{-}like\ carbon)}$ are shifted below CCO$_{(graphite)}$ and EMOG$_{(graphite)}$ by 0.08 log fO$_2$ units. At 3.5GPa, the possible reversed stability of glass-like carbon over graphite is shown, with CCO$_{(glass\text{-}like\ carbon)}$ and EMOG$_{(glass\text{-}like\ carbon)}$ located above CCO$_{(graphite)}$ and EMOG$_{(graphite)}$ by 0.01 log fO$_2$ units. In both cases, the difference of CCO curves pertaining to the two considered types of carbon is very small in terms of absolute fO$_2$ values. Nevertheless, as shown by our experimental results, these differences are enough to induce large variations in the composition of COH fluids interacting with crystalline versus glass-like solid carbon.

4.4. Comparison of glass-like carbon and glucose-derived char

Char synthesized for 24 h at 1 and 3GPa, 800 °C starting from glucose displays conchoidal fractures (Fig. 3c–f) and absence of cleavage, similar to glass-like carbon. Moreover,

Fig. 7. Thermodynamic properties of glass-like carbon. (A) glass-like carbon bulk modulus and its pressure dependence, compared with graphite. Measurements from Zhao et al. (2015) (green dots) are fitted with different K^0 and K'. The preferred model (red thick) assumes $K^0 = 9$GPa and $K' = 2.9$. See text for other details. (B) Gibbs free energy versus pressure at 800 °C, calculated using different thermodynamic models of glassy carbon. Red arrows indicate the shift of the preferred model assuming either an increased molar volume (i.e., lower density) or an increased compressibility (lower K^0). (C) difference in Gibbs free energy between glass-like carbon and graphite (ΔG), plotted as a function of pressure at $T = 800$ °C. Red thick (preferred model): $K^0 = 9$GPa, $K' = 2.9$, density (d) = 2.2.5 g/cm^3. Red dashed: $K^0 = 12$GPa, $K' = 2.9$, d = 2.25 g/cm^3. Purple dashed: $K^0 = 15$GPa, $K' = -2.4$, $d = 2.25$ g/cm^3. Orange dashed: $K^0 = 0.1$GPa, $K' = 6.3$, $d = 2.25$ g/cm^3. Green dashed: $K^0 = 9$GPa, $K' = 2.9$, $d = 1.5$ g/cm^3. Blue: diamond. Black thick: graphite. Light yellow field: thermodynamic stability of glass-like carbon (preferred model) over graphite and diamond. (For interpretation of the references to colour in this figure legend, the reader is referred to the web version of this article.)

Table 4
Thermodynamic properties of graphite and glass-like carbon (preferred model) at different pressures and temperatures. See also Supplementary Table 1 for a Perple_X formatted version including diamond.

P GPa	1.00E-04	1	3	1.00E-04	1	3
T °C	25 standard state	25	25	800	800	800
graphite						
$G_{P,T}$ kJ/mol	0.000	5.195	15.309	−12.866	−7.529	2.763
$S_{P,T}$ J/mol/K	5.74	5.64	5.49	26.04	25.88	25.61
$V_{P,T}$ J/mol/bar	0.53	0.52	0.50	0.54	0.53	0.50
$K_{P,T}$ GPa	33.8	42.8	60.6	30.1	39.1	57.0
K'	8.9	8.9	8.9	8.9	8.9	8.9
glass-like carbon (preferred model)						
$G_{P,T}$ kJ/mol	2.357	7.398	16.350	−11.142	−6.018	2.982
$S_{P,T}$ J/mol/K	6.60	6.53	6.53	26.90	26.77	26.69
$V_{P,T}$ J/mol/bar	0.53	0.48	0.42	0.54	0.49	0.42
$K_{P,T}$ GPa	9.0	11.9	17.6	8.0	10.8	16.5
K'	2.9	2.9	2.9	2.9	2.9	2.9
ΔG kJ/mol	2.357	2.203	1.041	1.724	1.511	0.219

Graphite parameters after Day (2012).
$\Delta G = G_{P,T}$ (glass-like carbon) $- G_{P,T}$ (graphite).
G_f^0 and S^0 of glass-like carbon: fit from Gutzow (2005) (G–T data at ambient pressure).
V^0 of glass-like carbon assumed indentical to graphite.
K^0 and K' of glass-like carbon: fit Zhao et al. (2014) (data at 25 °C from 1 to 3GPa; glass-like carbon type I).

char and glass-like carbon show broadly similar Raman spectra (Fig. 4), X-ray diffraction patterns (Supplementary Fig. 3) and nano-sized crystallite dimensions, supporting our experimental strategy in which glass-like carbon was chosen as the best analogue for disorganized, poorly crystalline carbonaceous organic matter. In this study, we observed a marked difference in Raman spectra acquired for char synthesized in 12-h and 24-h runs performed at 1GPa and 800 °C. In particular, the graphite G' peak at about 2700 cm^{-1}, well developed in the 12-h run, becomes only hinted in the 24-h run, suggesting that the size of the graphite crystallites decreased with time. This implies, in agreement with Beyssac et al. (2003), that the structure of char, although somewhat similar to glass-like carbon, is not stable at high-pressure/high-temperature conditions, and so this type of materials would be not suitable for long experiments at static equilibrium conditions. In this study, however, we observed transient near-equilibrium conditions between char and aqueous fluids generated by dehydration of glucose. Ideally, in perfectly closed systems, the thermal decomposition of anhydrous glucose (CH$_2$O) should produce carbon and pure water; however, this has been observed only in the run performed at 3GPa and 800 °C, containing almost pure water ($\approx$99 mol% H$_2$O). In fact, dehydration of glucose at 1GPa produced CH$_4$-rich, CO$_2$-bearing fluids after 12 h and CO$_2$-rich, CH$_4$-bearing fluids after 24 h. However, if the measured composition of these fluids is compared with those predicted by the modified model of Zhang and Duan (2009) implemented with the retrieved glass-like carbon equilibrium constants, both XCO$_2$ and XCH$_4$ ratios match redox conditions of ΔFMQ = −1.8, suggesting near-equilibrium conditions and a close thermodynamic affinity between glass-like carbon and char. In longer runs (24 h) at the same conditions

of 1GPa and 800 °C, measured XCO$_2$ and XCH$_4$ ratios correspond also in this case to consistent redox states (ΔFMQ = −1.2, if XCO$_2$ is considered; ΔFMQ = −1.0 if XCH$_4$ is taken into account). The measured fluid compositions suggest that the interaction with char in unbuffered single gold capsules evolves over time from reduced conditions, likely buffered by glucose (Hawkins, 1929; Kunz et al., 2011), to more oxidized conditions, likely constrained by the MgO–graphite–NaCl–Pyrex furnace assembly (close to FMQ; cf. Olafsson and Eggler, 1983). In agreement with previous studies (e.g., Truckenbrodt et al., 1997; Truckenbrodt and Johannes, 1999; Matjuschkin et al., 2014), we observed that unbuffered single gold capsules cannot therefore be considered systems perfectly closed to H$_2$O and H$_2$, so the buffering of the system (for instance using double capsules) is mandatory to constrain the H$_2$ (and, indirectly, the O$_2$) chemical potential.

4.5. Implications for organic matter dissolution at subduction zones

Organic matter can be an important constituent of oceanic sediments (Mayer et al., 1992), and on average it accounts for less than 1wt.% (Kelemen and Manning, 2015). Nevertheless, organic matter in deep-sea fans can dominate the carbon input flux at some margins (Plank and Manning, 2019). The proportion of organic to inorganic carbon (i.e., marine carbonates) subducted globally is about 20% (Plank and Manning, 2019) and the total amount of organic carbon subducted in modern active subduction zones is estimated > 11 Mt C/y (Clift, 2017). Once subducted and heated, poorly organized organic matter is progressively transformed into crystalline graphite through a multitude of intermediate stages generally referred to disordered gra-
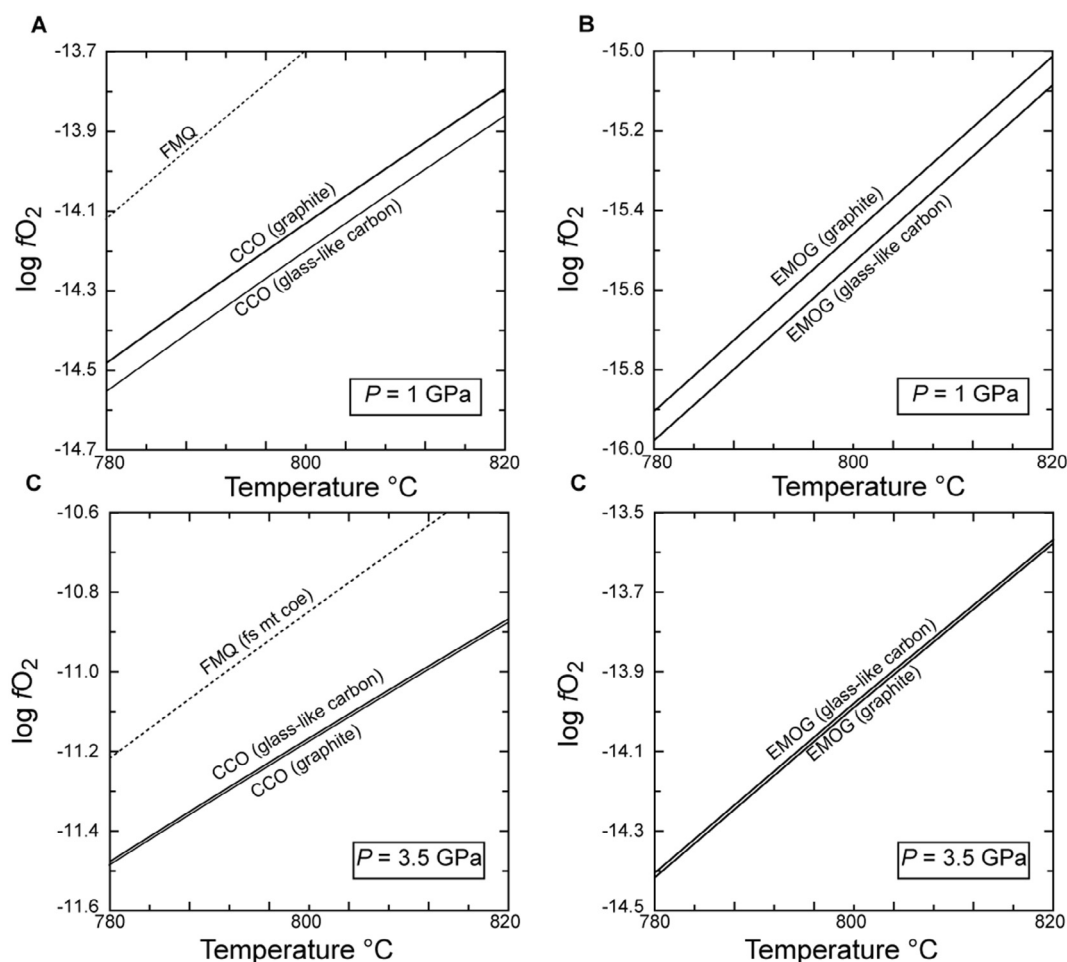
Fig. 8. Calculated T–log fO_2 diagrams of the univariant equilibria $C + O_2 = CO_2$ (CCO) and $MgSiO_3 + MgCO_3 = Mg_2SiO_4 + C + O_2$ (EMOG) involving graphite and glass-like carbon close to $T = 800$ °C at $P = 1$ GPa and at $P = 3.5$ GPa, using the thermodynamic properties reported in Table 4. FMQ: fayalite–magnetite-quartz or ferrosilite (fs)-magnetite (mt)-coesite (coes) oxygen buffer.

phitic carbon (Beyssac and Rumble, 2014; Buseck and Beyssac, 2014). In addition, graphite can also form by reduction of carbonates during subduction (Galvez et al., 2013; Vitale-Brovarone et al., 2017) and by precipitation from subduction C-O-H fluids (Luque et al., 1998).

The oxidation susceptibility and therefore the dissolution of graphite in aqueous fluids varies as a function of P, T and fO_2 conditions (e.g., Connolly, 1995; Tumiati and Malaspina, 2019). In general, low-temperature and high-pressure conditions characterizing subduction zones are thought to promote the stability of graphite, thus fluids interacting with this mineral should contain very low amounts of carbon and are essentially nearly pure water (Schmidt and Poli, 2013). However, we show in Fig. 9a that this is expected only at forearc conditions. In fact, at P–T conditions characterizing the slab surface (Syracuse et al., 2010), nearly pure water is expected only up to around 2 GPa and 450 °C. At greater depths, graphite-saturated fluids become progressively more enriched in CO_2 as FMQ and CCO buffers get very close (Fig. 9a), with maximum CO_2 contents ($XCO_2 = 0.55$) at subarc conditions (3 GPa–700 °C), where the two buffers nearly converge. These fluid compositions

are predicted assuming a perfectly crystalline and ordered state of graphite. Several previous studies suggested that the poorly ordered graphite might behave differently, in particular showing a higher solubility in aqueous fluids (Ziegenbein and Johannes, 1980; Connolly, 1995; Luque et al., 1998). Although our investigated P–T conditions are not strictly comparable with "normal" subduction regimes, especially at low pressures, we demonstrate that glass-like carbon is characterized by a marked difference in free energy (≈ 2 kJ/mol) with respect to crystalline graphite at low pressures, diminishing with increasing pressures and with a possible sign reversal close to graphite-diamond transition (located at 3.6 GPa and 760 °C in Fig. 9a). Because we show that the difference in free energy between graphite and glass-like carbon is predominantly due to their different compressibility behavior, the relative difference in carbon solubility depends only slightly on temperature. Therefore, we speculate that similar differences in fluid carbon content (in terms of $CO_{2(aq)}$, but possibly also of $CH_{4(aq)}$, HCO_3^{3-}, CO_3^{2-} and other dissolved C–O–H species at appropriate P–T–fO_2–fH_2–pH conditions) can be expected at lower temperatures characterizing the subduction zones and in particular the
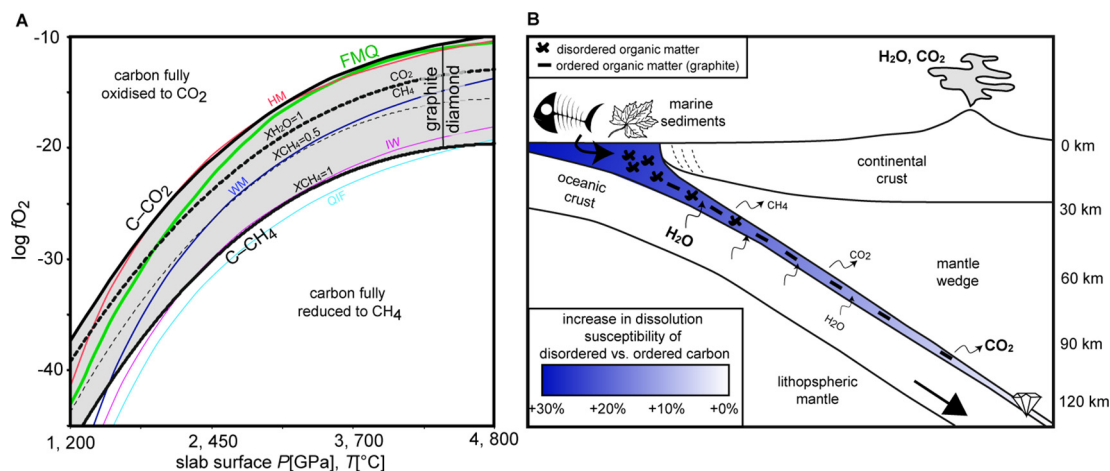
Fig. 9. Fate of organic matter in subduction. (A) Stability of COH fluids (grey field) calculated as a function of fO_2 along a subduction P–T gradient consistent with the average thermal model of slab surface after Syracuse et al. (2010). COH fluids are stable between the two boundaries $C + O_2 = CO_2$ (CCO) and $C + 2H_2 = CH_4$. At this scale, differences between graphite and amorphous carbon are negligible, but according to the preferred model in Fig. 7 glass-like carbon would be the stable carbon polymorph at $P > 3.4$ GPa. The calculation of fluid isopleths ($XCO_2 = CO_2/H_2O + CO_2$; $XCH_4 = CH_4/H_2O + CH_4$) has been performed using the Perple_X and the EoS of Connolly and Cesare (1993). Reference buffers FMQ, hematite-magnetite (HM), wustite-magnetite (WM), iron-wustite (IW) and quartz-iron-fayalite (QIF) are shown for reference. Fluids in equilibrium with graphite buffered at FMQ conditions become increasingly enriched in CO_2, which reaches its maximum concentration at about 100 km depth, where FMQ and CCO almost converge. (B) Cartoon showing the fate of organic matter in subduction zones. Disordered organic matter contained in marine sediments undergoes partial to complete graphitization by increasing subduction temperature. Experimental results and thermodynamic models presented in this study indicate that disordered carbon is more prone to oxidation with respect to crystalline carbon especially at low pressures, characterizing the forearc region. At these depths, an intense flush of water would be able to dissolve selectively disordered organic matter from the subducted sediments, while graphite behaves in a more refractory manner. This differential dissolution susceptibility is expected to progressively decrease as subduction proceeds, vanishing at about 100 km depth where the difference in free energy between graphite and disordered carbon tends to zero.

subduction surface where sediments containing organic matter can be abundant.

This implies that disordered graphitic carbon is more prone to oxidation relative to ordered crystalline graphite, resulting in fluids enriched in CO_2 compared to current estimates: the lower the pressure, the higher the differential dissolution susceptibility. Therefore, because it is unlikely that organic carbon can persist in its disordered state at great depths and consequent relatively high temperatures (Beyssac et al., 2002), and because the difference in free energy is higher at low pressures, we infer that the most important effect on carbon recycling concerns the shallowest levels of subduction zones, where disordered organic carbon can be expected to be far more reactive than graphite (Fig. 9b).

Obviously an important source of uncertainty arises from the assumption that glass-like carbon can be considered an analogue of disordered natural carbonaceous matter. Carbon materials are very complex because their properties change extensively with structural defects and impurities, and the type of hybridization, in particular sp^2 (graphite-like carbon) vs. sp^3 (diamond-like carbon) (e.g., Robertson, 2002; Langenhorst and Campione, 2019). Moreover, the activity and the reactivity of these materials can be modified by bringing them to nanosize dimensions. For instance, Guencheva et al. (2001) and Gutzow et al. (2005) showed that nanodispersed (10 nm) glass-like carbon displays a difference in Gibbs free energy compared to graphite of +12 kJ/mol at standard conditions, which is substantially higher relative to bulk glass-like carbon

(+2.4 kJ/mol; Table 4) and which would result in dissolution susceptibility higher than that provided in our study. In addition, natural highly disordered carbon, as synthetic amorphous and graphitic carbon, is likely characterized by a higher kinetic reactivity because of the presence of active immobilized free radicals (dangling bonds) and defects which make these materials efficient catalysts (e.g., Jüntgen, 1986). The results of our study therefore represent a first attempt to provide a conservative minimum estimate of the enhanced dissolution of disordered carbon with respect to crystalline graphite in natural systems.

5. CONCLUSIONS

Well-ordered crystalline graphite and X-ray amorphous glass-like carbon display different dissolution susceptibility in aqueous fluids, because of their different thermodynamic properties. On the basis of our experimental observations concerning this type of disordered sp^2 carbon, and aware of the uncertainties arising from the choice of glass-like carbon as an analogue materials for naturally occurring poorly organized carbon derived from the graphitization of organic matter, we may speculate at this stage that also natural poorly organized graphitic carbon could behave in a different manner compared to perfectly crystalline graphite. In particular, disordered carbonaceous matter could be more prone to dissolve in aqueous fluids compared to well-crystallized graphite especially at pressures corresponding to the forearc region of subduction zones. High

fluxes of water coming from the dehydration of the down-going slab would therefore induce an effective removal of organic matter from its sedimentary cover, prompting metasomatism of the mantle wedge (Sieber et al., 2018) and contributing to the global deep carbon cycle. As for glass-like carbon, the differential dissolution susceptibility declines with increasing pressure corresponding to 110 km depth, below which "disordered" carbon could be even less soluble than graphite. The stability of glass-like carbon relative to diamond, although predicted by the suggested model in the 3.7–4.2GPa pressure window, relies on thermodynamic parameters that are affected by uncertainties that are currently unquantifiable. The occurrence of nano-crystalline disordered graphitic carbon and amorphous sp^2 and sp^3 carbon has been indeed reported in micro- and nano-sized diamonds from Cignana Lake in the Western Alps (Frezzotti et al., 2014; Frezzotti, 2019) and glass-like X-ray amorphous carbon has been obtained experimentally at diamond-stable conditions (7.7GPa and 1000 °C; Yamaoka et al., 2002). However, more investigations are required to confirm this possibility.

Declaration of Competing Interest

The authors declared that there is no conflict of interest.

APPENDIX A. TERMINOLOGY USED FOR THE DESCRIPTION OF SOLID CARBON

In this study, the terminology used for the description of solid carbon follows the recommendations of IUPAC (Fitzer et al., 1995).

- Graphite: an allotropic form of the element carbon consisting of layers of hexagonally arranged carbon atoms in a planar condensed ring system (graphene layers). The layers are stacked parallel to each other in a three-dimensional crystalline long-range order. The chemical bonds within the layers are covalent with sp^2 hybridization.
- Graphitic carbon: all varieties of substances consisting of the element carbon in the allotropic form of graphite irrespective of the presence of structural defects. The use of the term is justified if three-dimensional hexagonal long-range order can be detected in the material by diffraction methods, independent of the volume fraction and the homogeneity of distribution of such crystalline domains.
- Glass-like carbon: in this study we use this term although the commercial/trademark terms "glassy carbon" and "vitreous carbon" are still widely used in experimental petrology and materials sciences papers. Glass-like carbon is agranular (i.e., homogenous microstructure with structural elements undistinguishable by optical microscopy) and non-graphitizable carbon (i..e, it does not convert into graphitic carbon upon heat treatment to 2500–3300 K) with a very high isotropy. Although its structure is not comparable to silicate glasses, the fracture surfaces have a pseudo-glassy (conchoidal) appearance. It consists of curved two-dimensional structural elements (graphene layers, i.e., single carbon layers of the graphite structure) dispersed in an X-ray amorphous matrix, but it does not exhibit dangling bonds that characterize the so-called "amorphous carbon". In fact, the term "amorphous carbon" is restricted to the description of carbon materials which, in addition to a lack of long-range crystalline order and to deviations of the interatomic distances with respect to graphite lattice as well as to the diamond lattice, show deviations in the bond angles because of the presence of dangling bonds. Amorphous carbon is disordered even on the atomic scale and have a fraction of sp^3 bonds ranging from a few ("graphite-like" structure) to almost 100% ("diamond-like" structure) (Sundqvist and Olabi, 2016)
- Char: a solid decomposition product of a natural or synthetic organic material. In this study, char is produced by carbonization (pyrolysis) of glucose. The term pyrolytic carbon has been avoided because it is restricted to carbon materials deposited from gaseous hydrocarbon compounds by chemical vapor deposition.

APPENDIX B. SUPPLEMENTARY MATERIAL

Supplementary data to this article can be found online at https://doi.org/10.1016/j.gca.2020.01.030.

REFERENCES

Aoya M., Kouketsu Y., Endo S., Shimizu H., Mizukami T., Nakamura D. and Wallis S. (2010) Extending the applicability of the Raman carbonaceous-material geothermometer using

data from contact metamorphic rocks. *J. Metamorph. Geol.* **28**(9), 895–914. https://doi.org/10.1111/j.1525-1314.2010.00896.x.

Bernard S., Benzerara K., Beyssac O., Menguy N., Guyot F., Brown G. E. and Goffé B. (2007) Exceptional preservation of fossil plant spores in high-pressure metamorphic rocks. *Earth Planet. Sci. Lett.* **262**, 257–272.

Beyssac O., Brunet F., Petitet J.-P., Goffé B. and Rouzaud J.-N. (2003) Experimental study of the microtextural and structural transformations of carbonaceous materials under pressure and temperature Available at:. *Eur. J. Mineral.* **15**, 937–951 http://www.ingentaselect.com/rpsv/cgi-bin/cgi?ini=xref&body=linker&reqdoi=10.1127/0935-1221/2003/0015-0937.

Beyssac O., Rouzaud J.-N., Goffé B., Brunet F. and Chopin C. (2002) Graphitization in a high-pressure, low-temperature metamorphic gradient: a Raman microspectroscopy and HRTEM study Available at:. *Contrib. Mineral. Petrol.* **143**, 19–31 http://link.springer.com/10.1007/s00410-001-0324-7.

Beyssac O. and Rumble D. (2014) Graphitic carbon: a ubiquitous, diverse, and useful geomaterial. *Elements* **10**, 415–420.

Bose K. and Ganguly J. (1995) Quartz-coesite transition revisited - Reversed experimental determination at 500–1200 °C and retrieved thermochemical properties. *Am. Mineral. Mineral.* **80**, 231–238.

Buseck P. R. and Beyssac O. (2014) From organic matter to graphite: graphitization. *Elements* **10**, 421–426.

Cappelletti R. L., Udovic T. J. and Paul R. L. (2018) Glassy carbon, NIST Standard Reference Material (SRM 3600): hydrogen content, neutron vibrational density of states and heat capacity. *J. Appl. Crystallogr.* **51**, 1323–1328.

Cartigny P., Stachel T., Harris J. W. and Javoy M. (2004) Constraining diamond metasomatic growth using C- and N-stable isotopes: examples from Namibia. *Lithos* **77**, 359–373.

Clift P. D. (2017) A revised budget for Cenozoic sedimentary carbon subduction. *Rev. Geophys.* **55**, 97–125.

Connolly J. A. D. (2005) Computation of phase equilibria by linear programming: a tool for geodynamic modeling and its application to subduction zone decarbonation. *Earth Planet. Sci. Lett.* **236**, 524–541.

Connolly J. A. D. (1995) Phase diagram methods for graphitic rocks and application to the system. *Contrib. Mineral. Petrol.*, 94–116.

Connolly J. A. D. and Cesare B. (1993) C-O-H-S fluid composition and oxygen fugacity in graphitic metapelites. *J. Metamorph. Geol.* **11**, 379–388.

Cowlard F. C. and Lewis J. C. (1967) Vitreous carbon – a new form of carbon. *J. Mater. Sci.* **2**, 507–512.

Dasgupta R., Hirschmann M. M. and Dellas N. (2005) The effect of bulk composition on the solidus of carbonated eclogite from partial melting experiments at 3 GPa. *Contrib. Mineral. Petrol.* **149**, 288–305.

Day H. W. (2012) A revised diamond-graphite transition curve. *Am. Mineral.* **97**, 52–62.

Duncan M. S. and Dasgupta R. (2017) Rise of Earth's atmospheric oxygen controlled by efficient subduction of organic carbon. *Nat. Geosci.* **10**, 387–392.

Eugster H. P. and Skippen G. B. (1967) Igneous and metamorphic reactions involving gas equilibria. *Res. Geochem.* **2**, 492–520.

Falloon T. J., Green D. H., Danyushevsky L. V. and Mcneill A. W. (2008) The composition of near-solidus partial melts of fertile peridotite at 1 and 1.5 GPa: Implications for the petrogenesis of MORB. *J. Petrol.* **49**, 591–613.

Ferrari A. C. (2007) Raman spectroscopy of graphene and graphite: disorder, electron-phonon coupling, doping and nonadiabatic effects. *Solid State Commun.* **143**, 47–57.

Ferrari A. C. and Robertson J. (2001) Resonant Raman spectroscopy of disordered, amorphous, and diamond-like carbon. *Phys. Rev. B* **64**, 075414.

Fitzer E., Köchling K. H., Boehm H. P. and Marsh H. (1995) Recommended terminology for the description of carbon as a solid. *Pure Appl. Chem.* **67**, 473–506.

Frezzotti M. L. (2019) Diamond growth from organic compounds in hydrous fluids deep within the Earth. *Nat. Commun.* **10**. https://doi.org/10.1038/s41467-019-12984-y 4952.

Frezzotti M. L., Huizenga J. M., Compagnoni R. and Selverstone J. (2014) Diamond formation by carbon saturation in C-O-H fluids during cold subduction of oceanic lithosphere. *Geochim. Cosmochim. Acta* **143**, 68–86. https://doi.org/10.1016/j.gca.2013.12.022.

Galvez M. E., Beyssac O., Martinez I., Benzerara K., Chaduteau C., Malvoisin B. and Malavieille J. (2013) Graphite formation by carbonate reduction during subduction. *Nat. Geosci.* **6**, 473–477. https://doi.org/10.1038/ngeo1827.

Guencheva V., Grantscharova E. and Gutzow I. (2001) Thermodynamic properties of the amorphous and crystalline modifications of carbon and the metastable synthesis of diamond. *Cryst. Res. Technol.* **36**, 1411–1428.

Gutzow I., Todorova S., Kostadinov L., Stoyanov E., Guencheva V., Völksch G., Dunken H. and Rüssel C. (2005) Diamonds by transport reactions with vitreous carbon and from the plasma torch: new and old methods of metastable diamond syhtnesis and growth. In *Nucleation theory and applications* (eds. J. W. P. Schmelzer and J. W. P. Schmelzer). Wiley-VCH Verlag, pp. 256–311.

Hammersley A. P. (1997) FIT2D: An Introduction and overview. *ESRF Internal Report*, ESRF97HA02T.

Hammersley A. P., Svensson S. O., Thompson A., Graafsma H. and Kvick Å. (1995) Calibration and correction of distorsions in two-dimensional detector systems. *Rev. Sci. Instrum.* **66**, 2729.

Hawkins J. A. (1929) Reducing powers of different sugars for the ferricyanide reagent used in the gasometric sugar method. *J. Biol. Chem.* **84**, 79–83.

Hayes J. M. and Waldbauer J. R. (2006) The carbon cycle and associated redox processes through time. *Philos. Trans. R. Soc. Lond. B. Biol. Sci.* **361**, 931–950.

Holland T. J. B. and Powell R. (1998) An internally consistent thermodynamic data set for phases pf petrological interest. *J. Metamorph. Geol.* **16**, 309–343.

Hu M., He J., Zhao Z., Strobel T. A., Hu W., Yu D., Sun H., Liu L., Li Z., Ma M., Kono Y., Shu J., Mao H., Fei Y., Shen G., Wang Y., Juhl S. J., Huang J. Y., Liu Z., Xu B. and Tian Y. (2017) Compressed glassy carbon: an ultrastrong and elastic interpenetrating graphene network. *Sci. Adv.* **3**, e1603213.

Huang F., Daniel I., Cardon H., Montagnac G. and Sverjensky D. A. (2017) Immiscible hydrocarbon fluids in the deep carbon cycle. *Nat. Commun.* **8**, 15798.

Huang F. and Sverjensky D. A. (2019) Extended Deep Earth Water Model for predicting major element mantle metasomatism. *Geochim. Cosmochim. Acta* **254**, 192–230. https://doi.org/10.1016/j.gca.2019.03.027.

Jüntgen H. (1986) Activated carbon as catalyst support. A review of new research results. *Fuel* **65**, 1436–1446.

Kelemen P. B. and Manning C. E. (2015) Reevaluating carbon fluxes in subduction zones, what goes down, mostly comes up 201507889. *Proc. Natl. Acad. Sci.* http://www.pnas.org/lookup/doi/10.1073/pnas.1507889112.

Kunz T., Lee E. J., Schiwek V., Seewald T. and Methner F. J. (2011) Glucose – a reducing sugar? Reducing properties of sugars in beverages and food. *Brew. Sci.* **64**, 61–67.

Langenhorst F. and Campione M. (2019) Ideal and real structures of different forms of carbon, with some remarks on their geological significance. *J. Geol. Soc. Lond.* **176**, 337–347.

Li Y. (2016) Immiscible C-H-O fluids formed at subduction zone conditions. *Geochem. Perspect. Lett.* **3**, 12–21 http://www.geo-chemicalperspectivesletters.org/article1702.

Luque F. J., Pasteris J. D., Wopenka B., Rodas M. and Barrenechea J. F. (1998) Natural fluid-deposited graphite: Mineralogical characteristics and mechanisms of formation. *Am. J. Sci.* **298**, 471–498.

Luth R. W. (1989) Natural versus experimental control of oxidation state : Effects on the composition and speciation of C-O-H fluids. *Am. Mineral.* **74**, 50–57.

Manning C. E., Shock E. L. and Sverjensky D. A. (2013) The chemistry of carbon in aqueous fluids at crustal and upper-mantle conditions: experimental and theoretical constraints. *Rev. Mineral. Geochemistry* **75**, 109–148 https://pubs.geo-scienceworld.org/rimg/article/75/1/109-148/140933.

Mason E., Edmonds M. and Turchyn A. V. (2017) Remobilization of crustal carbon may dominate volcanic arc emissions. *Science (80-.)* **357**, 290–294.

Matjuschkin V., Brooker R. A., Tattitch B., Blundy J. D. and Stamper C. C. (2014) Control and monitoring of oxygen fugacity in piston cylinder experiments. *Contrib. Mineral. Petrol.* **169**, 1–16.

Mattioli G. S. and Wood B. J. (1988) Magnetite activities across the $MgAl_2O_4$-Fe_3O_4 spinel join, with application to thermo-barometric estimates of upper mantle oxygen fugacity. *Contrib. Mineral. Petrol.* **98**, 148–162.

Matveev S., Ballhaus C., Fricke K., Truckenbrodt J. and Ziegenben D. (1997) Volatiles in the Earth's mantle: I. Synthesis of CHO fluids at 1273 K and 2.4 GPa. *Geochim. Cosmochim. Acta* **61**, 3081–3088.

Mayer L., Pisias N. and Janacek T. (1992) 14. SITE 849. *Proc. Ocean Drill. Program. Initial Rep.* **138**, 735–807.

McCollom T. M. (2013) Laboratory simulations of abiotic hydro-carbon formation in Earth's deep subsurface. *Rev. Mineral. Geochem.* **75**, 467–494. https://doi.org/10.2138/rmg.2013.75.15.

O'Neill H. S. C. and Pownceby M. I. (1993) Thermodynamic data from redox reactions at high temperatures. I. An experimental and theoretical assessment of the electrochemical method using stabilized zirconia electrolytes, with revised values for the Fe-"FeO", Co-CoO, Ni-NiO and Cu-Cu_2O oxygen buffers, and new data for the W-WO_2 buffer. *Contrib. Mineral. Petrol.* **114**, 296–314 http://link.springer.com/article/10.1007/BF01046533.

Olafsson M. and Eggler D. H. (1983) Phase relations of amphibole, amphibole-carbonate, and phlogopite-carbonate peridotite: petrologic constraints on the asthenosphere. *Earth Planet. Sci. Lett.* **64**, 305–315.

Palot M., Pearson D. G., Stern R. A., Stachel T. and Harris J. W. (2014) Isotopic constraints on the nature and circulation of deep mantle C-H-O-N fluids: carbon and nitrogen systematics within ultra-deep diamonds from Kankan (Guinea). *Geochim. Cosmochim. Acta* **139**, 26–46. https://doi.org/10.1016/j.gca.2014.04.027.

Pan D. and Galli G. (2016) The fate of carbon dioxide in water-rich fluids under extreme conditions. *Sci. Adv.* **2**, e1601278. https://doi.org/10.1126/sciadv.1601278.

Pasteris J. D. (1989) Analysis in geological thin-sections by Laser Raman Microprobe Spectroscopy: A cautionary note. *Appl. Spectrosc.* **43**(3), 567–570.

Plank T. and Manning C. E. (2019) Subducting carbon. *Nature* **574**, 343–352. https://doi.org/10.1038/s41586-019-1643-z.

Ponschke M. A. and House J. E. (2011) Kinetic studies on the loss of water from α-d-glucose monohydrate. *Carbohydr. Res.* **346**, 2285–2289. https://doi.org/10.1016/j.carres.2011.07.012.

Robertson J. (2002) Diamond-like amorphous carbon. *Mater. Sci. Eng. Rep.* **37**, 129–281.

Robinson J. A. C., Wood B. J. and Blundy J. D. (1998) The beginning of melting of fertile and depleted peridotite at 1.5 GPa. *Earth Planet. Sci. Lett.* **155**, 97–111.

Schmidt M. W. and Poli S. (2013) Devolatilization during subduction 2nd ed.. *Treatise Geochemistry* **4**, 669–701. https://doi.org/10.1016/B978-0-08-095975-7.00321-1.

Shiell T. B., McCulloch D. G., McKenzie D. R., Field M. R., Haberl B., Boehler R., Cook B. A., De Tomas C., Suarez-Martinez I., Marks N. A. and Bradby J. E. (2018) Graphiti-zation of glassy carbon after compression at room temperature. *Phys. Rev. Lett.* **120**, 215701. https://doi.org/10.1103/PhysRevLett.120.215701.

Sieber M. J., Hermann J. and Yaxley G. M. (2018) An experimental investigation of C–O–H fluid-driven carbonation of serpentinites under forearc conditions. *Earth Planet. Sci. Lett.* **496**, 178–188. https://doi.org/10.1016/j.epsl.2018.05.027.

Spandler C., Yaxley G., Green D. H. and Rosenthal A. (2008) Phase relations and melting of anhydrous K-bearing eclog-ite from 1200 to 1600°C and 3 to 5 GPa. *J. Petrol.* **49**, 771–795.

Stachel T., Harris J., Aulbach S. and Deines P. (2002) Kankan diamonds (Guinea) III: $\delta^{13}C$ and nitrogen characteristics of deep diamonds. *Contrib. to Mineral. Petrol.* **142**, 465–475.

Sundqvist B. and Olabi A. G. (2016) Fullerites and hard carbons. *Ref. Modul. Mater. Sci. Mater. Eng.*.

Sverjensky D. A., Harrison B. and Azzolini D. (2014a) Water in the deep Earth: The dielectric constant and the solubilities of quartz and corundum to 60kb and 1200°C. *Geochim. Cosmochim. Acta* **129**, 125–145 http://linkinghub.elsevier.com/retrieve/pii/S0016703713007151.

Sverjensky D. A., Stagno V. and Huang F. (2014b) Important role for organic carbon in subduction-zone fluids in the deep carbon cycle. *Nat. Geosci.* **7**, 909–913 http://www.nature.com/doifinder/10.1038/ngeo2291.

Syracuse E. M., van Keken P. E., Abers G. A., Suetsugu D., Bina C., Inoue T., Wiens D. and Jellinek M. (2010) The global range of subduction zone thermal models. *Phys. Earth Planet. Inter.* **183**, 73–90.

Takahashi Y. and Westrum E. F. J. (1970) Glassy carbon low-temperature themodynamic properties. *J. Chem. Thermodyn.* **2**, 847–854.

Tiraboschi C., Tumiati S., Recchia S., Miozzi F. and Poli S. (2016) Quantitative analysis of COH fluids synthesized at HP-HT conditions: an optimized methodology to measure volatiles in experimental capsules. *Geofluids* **16**, 841–855. https://doi.org/10.1111/gfl.12191.

Tiraboschi C., Tumiati S., Sverjensky D., Pettke T., Ulmer P. and Poli S. (2018) Experimental determination of magnesia and silica solubilities in graphite-saturated and redox-buffered high-pressure COH fluids in equilibrium with forsterite + enstatite and magnesite + enstatite. *Contrib. Mineral. Petrol.* **173**, 2 http://link.springer.com/10.1007/s00410-017-1427-0.

Toby B. H. (2001) EXPGUI, a graphical user interface for GSAS. *J. Appl. Cryst.* **34**, 210–213.

Truckenbrodt J. and Johannes W. (1999) H_2O loss during piston-cylinder experiments. *Am. Mineral.* **84**, 1333–1335.

Truckenbrodt J., Ziegenbein D. and Johannes W. (1997) Redox conditions in piston cylinder apparatus: the different behavior of boron nitride and unfired pyrophillite assemblies. *Am. Mineral.* **82**, 337–344.

Tumiati S. and Malaspina N. (2019) Redox processes and the role of carbon-bearing volatiles from the slab–mantle interface to the mantle wedge. *J. Geol. Soc. London.* **176**, 388–397. https://doi.org/10.1144/jgs2018-046.

Tumiati S., Tiraboschi C., Sverjensky D. A., Pettke T., Recchia S., Ulmer P., Miozzi F. and Poli S. (2017) Silicate dissolution boosts the CO_2 concentrations in subduction fluids. *Nat. Commun.* **8**, 616.

Vitale Brovarone A., Martinez I., Elmaleh A., Compagnoni R., Chaduteau C., Ferraris C. and Esteve I. (2017) Massive production of abiotic methane during subduction evidenced in metamorphosed ophicarbonates from the Italian Alps. *Nat. Commun.* **8**, 14134 http://www.nature.com/doifinder/10.1038/ncomms14134.

Wasylenki L. E. (2003) Near-solidus melting of the shallow upper mantle: partial melting experiments on depleted peridotite. *J. Petrol.* **44**, 1163–1191.

Yamaoka S., Shaji Kumar M. D., Kanda H. and Akaishi M. (2002) Crystallization of diamond from CO_2 fluid at high pressure and high temperature. *J. Cryst. Growth* **234**, 5–8. https://doi.org/10.1016/S0022-0248(01)01678-5.

Yokoyama J., Murabayashi M., Takahashi Y. and Mukaibo T. (1971) Measurement of high-temperature thermal properties of glassy carbon by laser flash method. *TANSO*, 44–47 (in Japanese).

Zhang C. and Duan Z. (2009) A model for C-O-H fluid in the Earth's mantle. *Geochim. Cosmochim. Acta* **73**, 2089–2102. https://doi.org/10.1016/j.gca.2009.01.021.

Zhang C. and Duan Z. (2010) GFluid: An Excel spreadsheet for investigating C-O–H fluid composition under high temperatures and pressures. *Comput. Geosci.* **36**, 569–572 http://linkinghub.elsevier.com/retrieve/pii/S0098300409002751.

Zhang S., Ague J. J. and Vitale Brovarone A. (2018) Degassing of organic carbon during regional metamorphism of pelites, Wepawaug Schist, Connecticut, USA. *Chem. Geol.* **490**, 30–44. https://doi.org/10.1016/j.chemgeo.2018.05.003.

Zhao Z., Wang E. F., Yan H., Kono Y., Wen B., Bai L., Shi F., Zhang J., Kenney-Benson C., Park C., Wang Y. and Shen G. (2015) Nanoarchitectured materials composed of fullerene-like spheroids and disordered graphene layers with tunable mechanical properties. *Nat. Commun.* **6**, 1–10. https://doi.org/10.1038/ncomms7212.

Ziegenbein D. and Johannes W. (1980) Graphite in C-H-O fluids: an unsuitable compound to buffer fluid composition at temperatures up to 700°C. *Neues Jahrb. fur Mineral. Monatshefte* **7**, 289–305.

Associate editor: Rajdeep Dasgupta